On the Mechanics of Natural Compliance in Frictional Contacts and its Effect on Grasp Stiffness and Stability

Amir Shapiro*
Dept. of ME
Ben Gurion University
ashapiro@bgu.ac.il

Elon Rimon
Dept. of ME
Technion
rimon@technion.ac.il

Alon Ohev-Zion
Dept. of ME
Ben Gurion University
alonohev@bgu.ac.il

Abstract *This paper considers the effect of natural material compliance on the stiffness and stability of frictional multi-contact grasps and fixtures. The contact preload profile is a key parameter in the nonlinear compliance laws governing such contacts. The paper introduces the Hertz-Walton contact compliance model which is valid for linear contact loading profiles. The model is specified in a lumped parameter form suitable for on-line grasping applications, and is entirely determined by the contact friction and by the material and geometric properties of the contacting bodies. The model predicts an asymmetric stiffening of the tangential reaction force as the normal load at the contact increases. As a result, the composite stiffness matrix of multi-contact grasps governed by natural compliance effects is asymmetric, indicating that these contact arrangements are not governed by any potential energy function. Based on the compliant grasp dynamics, the paper derives rules indicating which contact point locations and what preload profiles guarantee grasp and fixture stability. The paper also describes preliminary experiments supporting the contact model predictions.*

1 Introduction

This paper considers the effect of natural material compliance on frictional multi-contact arrangements. Natural friction-compliance effects play a key role in several grasping applications. For instance, biomimetic multi-finger hands are currently being developed for handling delicate objects such as fruits and vegetables [5, 43]. Such hands are typically designed with soft fingertips [3, 31], and the determination of grasp stability during object handling is a key component of these systems [27, 39, 50]. Natural contact compliance also plays an important

*Corresponding author: Dept. of ME, Ben Gurion University, Beer-Sheva, Israel.

role in quasistatic locomotion synthesis. When a multi-limb or snake-like robot moves quasistatically by embracing against the environment, natural force-displacement laws at the contacts influence the mechanism's overall stability [33, 35]. A similar observation holds for whole arm manipulation, where a robot arm is allowed to establish mid-link contacts with the manipulated object [12, 30]. Due to the passive nature of the mid-link contacts, the stability of whole-arm grasps requires a consideration of the natural friction-compliance laws at the contacts [48]. Industrial fixturing may also benefit from friction-compliance stability models. Current fixturing practice immobilizes a given workpiece using redundant form closure grasps (e.g. [4, 17]). This costly and time consuming practice relies on frictionless rigid-body constraints imposed by the fixturing elements [2, 16]. Sound understanding how material compliance affects the stiffness and stability of multi-contact arrangements may lead to more economic fixtures that use a smaller number of contacts.

The natural stiffness and stability of multi-contact arrangements is determined by nonlinear compliance laws. When these laws model frictional compliant contacts, they require explicit consideration of the contact loading profiles. The existing compliance models require that the contacts be preloaded only along the contact normals. This paper introduces the Hertz-Walton compliance model which allows any linear loading of the contacts. The existing compliance models determine the stability of a candidate grasp by constructing a potential energy function and computing its Hessian matrix. While a potential-function approach may be justified under normal loading profiles, this paper establishes that under general linear loading profiles the resulting grasp is *not* governed by any potential energy function. Using the Hertz-Walton model, the paper characterizes the stiffness and stability of multi-contact grasps preloaded along general linear loading profiles. In addition, the paper derives rules indicating which contact force magnitudes and linear loading profiles guarantee stable grasps.

The relevant literature can be divided into compliance models proposed in the solid mechanics literature, and compliant grasp synthesis tools developed in the robotics literature. In the solid mechanics literature, the modeling of the *normal* force due to material compliance effects is based on the classical Hertz model [14]. The main effort on modeling *tangential* material compliance at a non-slipping frictional contact is by Mindlin and Deresiewicz [25, 26]. They investigated the case where a contact is preloaded along the normal direction in accordance with the Hertz compliance model. Then they analyzed the tangential traction field generated by applying pure tangential loads while the normal load remains constant. Their investigation revealed highly nonlinear and complex phenomena such as micro-slip and hysteresis. Moreover, researchers in this field have come to realize that the tangential force-displacement law depends on the contact loading profile [20][p. 221]. Motivated by granular material packing applications, Walton [45] derived an analytic tangential compliance model which is much more relevant for grasping and fixturing applications. This model was later refined by Elata and Berryman [7]. Walton assumes that a contact is loaded along some

linear loading profile. Under this assumption (and using a different analysis approach than Mindlin's), he derived an analytic model for the tangential compliance force at a frictional contact. The normal force component in Walton's model satisfies the Hertz law, and the combined Hertz-Walton model is the basis for the investigation conducted in this paper. The solid mechanics literature also offers numerical compliance models based on finite-element analysis (e.g. [8, 49]). However, analytic lumped-parameter models provide the insight and computational simplicity required for automated grasp and fixture planning [19, 22].

In the robotics literature, the stability of compliant multi-contact grasps is determined by the grasp *stiffness matrix*. This matrix gives the linearized relation between small movements of the grasped object and the net reaction wrench (force and torque) generated by the contacts. Early papers model material compliance by linear springs that act in tandem with a rigid-body Coulomb friction law [1, 10]. A positive definite Hessian matrix of the springs' elastic potential energy ensures stability of such grasps [29, 47]. However, the linear spring approach is not supported by the solid mechanics literature. In particular, without knowledge of an underlying nonlinear contact model there is no way to predict the linear spring coefficients. Moreover, it is intuitively clear (and rigorously justified below) that the contacts experience tangential stiffening as the bodies are pressed harder together. Subsequent papers focused on the inclusion of the Hertz normal compliance model into the analysis and synthesis of *frictionless* grasps and fixtures [18, 23, 24, 50]. Systematic efforts at incorporating *frictional* compliance effects were made by Sinha and Abel [37], Li and Melkote [22], and Wang and Kumar [46]. However, these papers propose discretized friction-compliance contact models akin to the finite-element approach of the solid mechanics literature.

This paper emphasizes the use of analytic compliance models that allow closed form analysis and synthesis of stable grasps. Analytic compliance models have been proposed by Hirai et al. [19] and Xiong et al. [48]. Hirai et al. model soft fingertips as a continuoum of linear springs aligned with the finger's initial contact normal [19]. Based on the fingertip shape, they derive a power low which describes the elastic potential energy stored in the compressed fingertip. The potential energy associated with several fingertips was subsequently used to synthesize stable manipulation plans. Xiong et al. combined Sinha and Abel's contact model with the Hertz normal compliance model [48]. They obtained a nonlinear compliance model which predicts the normal and tangential contact reaction forces, and applied this model to the prediction of stability and force closure in whole-arm grasps. Our paper complements the existing papers in three fundamental ways. First, the existing compliance models require that the contacts be preloaded only along the contact normals. The Hertz-Walton model discussed in this paper allows any linear loading of the contacts. Second, the existing papers use the Hessian matrix of the grasp potential energy function to determine grasp stability. This paper establishes that under general linear loading profiles the resulting grasp is *not* governed by any potential energy function. The paper derives

the grasp's non-symmetric stiffness matrix and then determines which linear loading profiles guarantee grasp stability. The paper emphasizes the role of the contact loading profile in ensuring grasp stability, a topic which has not yet been discussed in the robotics literature.

The paper is structured as follows. Section 2 describes the Hertz-Walton compliance model associated with linear contact loading profiles. Section 3 derives the stiffness matrix at the individual contacts, which is shown to be *asymmetric* under the Hertz-Walton model. Section 3 characterizes which linear loadings profiles guarantee stable response at the individual contacts. Section 4 derives the composite grasp stiffness matrix associated with the Hertz-Walton model. The grasp stiffness matrix is *asymmetric,* thus indicating that the dynamics of such grasps is *not* governed by a potential energy function. To establish the stability of these grasps, Section 4 derives a criterion for compliantly stable grasps. Based on the stability criterion, Section 5 discusses guidelines for selecting the contact point locations and the loading profiles which give compliantly stable grasps. Section 6 describes experiments which validate the Hertz-Walton model for a single compliant fingertip. The concluding section discusses future research topics, most notably the need to validate the model stiffness and stability predictions in multi-finger settings.

2 Friction-Compliance Models

This section describes the Hertz and Walton compliance models in a configuration-space setting. Assume that a 3D object, $\mathcal{B}$, is held by stationary 3D bodies $\mathcal{A}_1, \ldots, \mathcal{A}_k$ representing fingertips or fixels. The usual assumption made in the solid mechanics literature is that the contacting bodies are *quasi-rigid*, meaning that their deformation due to material compliance is localized at the contacts [20]. This assumption is generally valid for bodies which are not made of exceptionally soft material and do not contain slender substructures [50]. The quasi-rigidity assumption allows us to describe the overall motion of $\mathcal{B}$ relative to the stationary bodies $\mathcal{A}_1, ..., \mathcal{A}_k$ using rigid body kinematics. Since the grasping bodies are essentially stationary, one can focus on $\mathcal{B}$'s configuration space, or *c-space.*

This paper considers the nonlinear contact compliance models in the context of planar configuration spaces. We assume that the bodies lie on a frictionless horizontal plane, such that the bodies interact via frictional forces parallel to the supporting plane.[1] The planar configuration of $\mathcal{B}$ is parametrized by $q = (d, \theta) \in \mathbb{R}^2 \times \mathbb{R}$, where d and θ are $\mathcal{B}$'s position and orientation relative to a fixed reference frame. The velocity of $\mathcal{B}$ is denoted $\dot{q} = (v, \omega) \in \mathbb{R}^2 \times \mathbb{R}$, where v and ω are $\mathcal{B}$'s linear and angular velocities. The wrenches acting on $\mathcal{B}$ are denoted $\boldsymbol{w} = (f, \tau) \in \mathbb{R}^2 \times \mathbb{R}$, where f and τ are the force and torque acting on $\mathcal{B}$. Note that $\boldsymbol{w}$ acts

[1] The object $\mathcal{B}$ is assumed to be influenced only by the finger bodies $\mathcal{A}_1, ..., \mathcal{A}_k$. The inclusion of other external influences such as gravity lie beyond the scope of this paper.

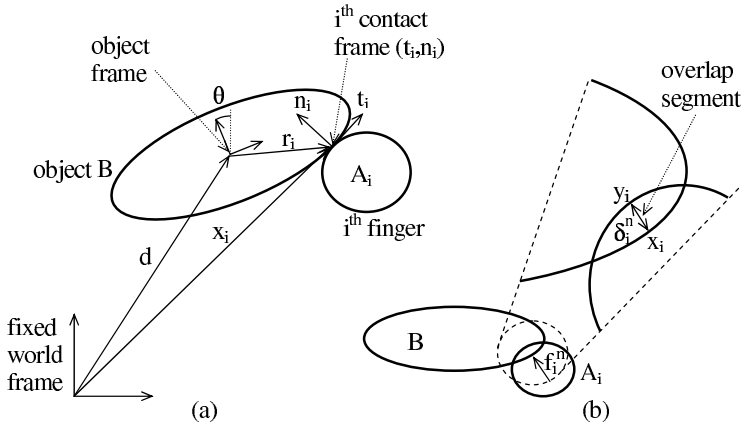

Figure 1: (a) The parametrization of $\mathcal{B}$'s c-space by (d, θ). (b) The overlap segment between $\mathcal{B}$ and $\mathcal{A}_i$ and the net normal force acting along this segment.

as a covector on $\dot{q}$, with $\boldsymbol{w} \cdot \dot{q}$ corresponding to the physical power transmitted to $\mathcal{B}$ during its instantaneous motion along $\dot{q}$.

2.1 Normal Compliance Models

Let us first describe a generic normal compliance modeling approach which ignores the details of compliant surface deformation and models the resultant contact force as a function of $\mathcal{B}$'s configuration [23]. Consider a single contact between $\mathcal{B}$ and $\mathcal{A}_i$. In the absence of deformation, the two bodies contact at a single point. When pushed together, the two contacting surfaces deform. One can conceptually think of the two rigid bodies as interpenetrating, or overlapping with their undeformed shapes, as illustrated in Figure 1(b). When $\mathcal{B}$ is located at a configuration q, the *overlap*[2] between $\mathcal{B}$ and $\mathcal{A}_i$, denoted $\delta_i^n(q)$, is the minimum amount of translation (with fixed orientation) of $\mathcal{B}$ that would separate it from $\mathcal{A}_i$. The *overlap segment* is the unique segment whose endpoints lie on the surfaces of $\mathcal{B}$ and $\mathcal{A}_i$, such that the length of the segment is δ_i^n and its direction is collinear with the direction of separating translation. For sufficiently small δ_i^n, the overlap segment is collinear with the normals to the surfaces of $\mathcal{B}$ and $\mathcal{A}_i$. In this lumped parameter form of modeling, the net normal force induced by the local deformation is assumed to act at $\mathcal{B}$'s endpoint of the overlap segment, x_i, along the inward pointing direction of the overlap segment, n_i (Figure 1). The normal component of the contact force, f_i^n, is assumed to depend on δ_i^n in terms of a function $g_i(\delta_i^n)$. This function is required to be differentiable, zero when δ_i^n is zero, and monotonically increasing when δ_i^n is positive. The normal component of the

[2]The notion of overlap is consistent with the concept of "relative approach" in contact mechanics [20].

contact force, f_i^n, obeys a generic law of the form:

$$f_i^n = g_i(\delta_i^n) + \delta_i^n \cdot \varphi_i^n(\dot{\delta}_i^n) \qquad \text{as long as } f_i^n > 0, \tag{1}$$

where $g_i'(\delta_i^n) > 0$ when $\delta_i^n > 0$. It is important to note that a wide variety of contact models can be represented under this generic law. The simplest contact model assumes that g_i is a linear function of the overlap, $g_i(\delta_i^n) = \kappa_i \delta_i^n$, where the coefficient κ_i represents the combined stiffness of $\mathcal{B}$ and $\mathcal{A}_i$ at the contact [18]. The function $\varphi_i^n(\dot{\delta}_i^n)$ represents damping due to viscoelastic effects [9, 21]. It is required to be differentiable, zero when $\dot{\delta}_i^n$ is zero, and monotonically increasing in $\dot{\delta}_i^n$. The damping force acts along $\mathcal{B}$'s inward contact normal when $\varphi_i^n > 0$. Hence it resists $\mathcal{B}$'s penetration into $\mathcal{A}_i$ when $\dot{\delta}_i^n > 0$, and it resists $\mathcal{B}$'s motion away from $\mathcal{A}_i$ when $\dot{\delta}_i^n < 0$. In the latter case the model (1) is valid as long as the net normal force remains positive, as required by the unilateral nature of this force. This requirement holds in a small neighborhood of any equilibrium state of $\mathcal{B}$, since $\dot{\delta}_i^n = 0$ implies that $\varphi_i^n = 0$ at any zero-velocity state. This observation will allow us to establish grasp stability in Section 4.

The Hertz normal compliance model [14]: The nonlinear Hertz model which has been verified experimentally [20], establishes that for two quasi-rigid bodies $\mathcal{A}_i$ and $\mathcal{B}$ with spherical tips of radii $r_{\mathcal{A}_i}$ and $r_{\mathcal{B}_i}$:

$$g_i(\delta_i^n) = \tfrac{8G\sqrt{r_i}}{3(1-\nu)}(\delta_i^n)^{3/2}, \tag{2}$$

where $r_i = r_{\mathcal{A}_i} r_{\mathcal{B}_i}/(r_{\mathcal{A}_i} + r_{\mathcal{B}_i})$, G is the material modulus of rigidity expressed in N/m^2, and ν is the material Poisson ratio. The Poisson ratio is a unitless parameter satisfying $0 \leq \nu \leq 0.5$ for all practical materials [20]. The Hertzian law is sometimes expressed in terms of the material modulus of elasticity, E, rather than G, where $E = 2G(1+\nu)$.

2.2 Tangential Compliance Models

The process underlying tangential compliance at a frictional contact is as follows. When two quasi-rigid bodies are preloaded along the normal direction, they locally deform and establish a contact area centered at the original contact point (Figure 2(a)). The deformed bodies generate a normal force-field which is continuously distributed along the contact area (its integral over the contact area gives the net normal force f_i^n). When the two bodies are next loaded along a tangential direction, they locally deform in a way that generates a tangential force-field which is again continuously distributed along the contact area (Figure 2(b)). The usual assumption made in the solid mechanics literature is that *the normal and tangential force fields interact at the individual points of the contact area according to Coulomb's*

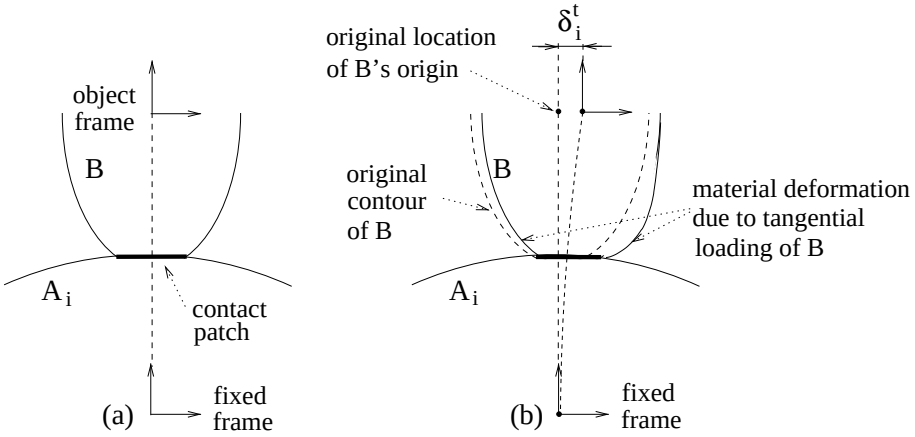

Figure 2: (a) An initial contact area generated by normal loading of $\mathcal{B}$ against $\mathcal{A}_i$. (b) Tangential loading of $\mathcal{B}$ causes tangential displacement of $\mathcal{B}$ without any macro-slip.

law [26]. Under this assumption, elasticity theory as well as experiments indicate that the tangential force-field consists of two regimes. At points in an outer ring of the contact area the tangential forces exceed the friction cone constraint, causing micro-slip at these points. At points along the complementary inner disc of the contact area the tangential forces lie within the friction cone, and at these points no micro-slip takes place. As the magnitude of the tangential loading increases the area of the stationary inner disc shrinks. Finally, when the net tangential force reaches μf_i^n (μ being the coefficient of friction), the inner disc shrinks to a point and the two bodies experience macro-slip at the contact.

Based on this insight, we formulate a generic tangential compliance law, assuming that the contacting bodies deform but do not slip. This law covers most of the tangential compliance models proposed in the literature [7, 26, 44, 45], and is therefore quite general. Recall that x_i is $\mathcal{B}$'s endpoint of the overlap segment. Let r_i denote the same point expressed in $\mathcal{B}$'s body frame (Figure 1(a)). Then x_i is related to r_i by the rigid-body transformation: $x_i = X(r_i, q) = R(\theta)r_i + d$, where $R(\theta)$ is $\mathcal{B}$'s orientation matrix. Let $X_{r_i}(q)$ denote the transformation $X(r_i, q)$ such that r_i is held fixed. When $\mathcal{B}$ moves along a c-space trajectory $q(t)$, the velocity of X_{r_i} is given by $\frac{d}{dt}X_{r_i}(q(t)) = G_i\dot{q}(t)$, where $G_i = DX_{r_i}$ is the 2×3 Jacobian matrix of X_{r_i}. Let $\delta_i^t(q(t))$ denote the tangential displacement of $\mathcal{B}$ relative to the i^{th} contact due to $\mathcal{B}$'s motion along $q(t)$ (Figure 2(b)). Let t_i denote the unit tangent to $\mathcal{B}$'s boundary at x_i. The derivative of δ_i^t along $q(t)$ is given by the projection of $\dot{X}_{r_i}$ along t_i:

$$\frac{d}{dt}\delta_i^t(q(t)) = t_i \cdot \dot{X}_{r_i} = t_i \cdot G_i\dot{q}(t). \tag{3}$$

In contrast with $\delta_i^n(q)$, the tangential displacement is *not* a direct function of q, but requires integration of (3) over the entire loading trajectory [20][p. 221]. The tangential component of the contact force, f_i^t, obeys a generic law of the form:

$$f_i^t = -h_i(\delta_i^t, \delta_i^n) - \delta_i^n \cdot \varphi_i^t(\dot{\delta}_i^t) \qquad \text{as long as } f_i^n > 0 \text{ and } |f_i^t| < \mu f_i^n, \tag{4}$$

where μ is the coefficient of friction. Note that the function representing the elastic component of the tangential force, $h_i(\delta_i^t, \delta_i^n)$, depends both on the tangential and normal displacements. This function is required to be differentiable, zero when δ_i^n is zero, and for any fixed positive δ_i^n monotonically increasing in δ_i^t. The negative sign preceding h_i in (4) implies that the tangential force *opposes* the direction of tangential displacement. The function $\varphi_i^t(\dot{\delta}_i^t)$ represents damping due to micro-slip. It is required to be differentiable, zero when $\dot{\delta}_i^t$ is zero, and monotonically increasing in $\dot{\delta}_i^t$. The negative sign preceding φ_i^t in (4) indicates that its force resists the instantaneous change in δ_i^t.

The Walton tangential compliance model [44, 45]: Walton assumes that a contact is loaded along a linear loading profile satisfying $\delta_i^t = c_i \delta_i^n$, such that c_i is constant throughout the loading process. When two quasi-rigid bodies $\mathcal{A}_i$ and $\mathcal{B}$ with spherical tips of radii $r_{\mathcal{A}_i}$ and $r_{\mathcal{B}_i}$ are preloaded with a linear loading profile, the function h_i is given by

$$\begin{aligned} h_i(\delta_i^t, \delta_i^n) &= \tfrac{16G\sqrt{r_i}}{3(2-\nu)} \sqrt{\delta_i^n}\, \delta_i^t \\ &\qquad \text{as long as } \delta_i^n > 0 \text{ and } |c_i| < \mu \tfrac{(2-\nu)}{2(1-\nu)}, \end{aligned} \tag{5}$$

where G and ν are specified above, $r_i = r_{\mathcal{A}_i} r_{\mathcal{B}_i} / (r_{\mathcal{A}_i} + r_{\mathcal{B}_i})$, and μ is the friction coefficient at the contact. The condition $|c_i| < \mu(2-\nu)/2(1-\nu)$ results from substituting formulas (2) and (5) for f_i^n and f_i^t in the friction cone constraint $|f_i^t| < \mu f_i^n$. Walton's formula is highly relevant for grasping and fixturing applications, since one can readily implement a linear preloading of the contacts. Note that (5) indicates a nonlinear tangential stiffening at the contact for larger normal penetrations. Walton's formula agrees up to constants with the tangential compliance model obtained by Mindlin and Deresiewicz [25, 26]. However, the Mindlin and Deresiewicz model assumes pure normal loading followed by pure tangential loading, while the Walton model allows any linear loading profile.

3 The Individual Contact Stiffness Matrices

The stability of a quasi-rigid object $\mathcal{B}$ held in a compliant equilibrium grasp is determined by the net wrench induced on $\mathcal{B}$ by the contacts in response to small object displacements.

This section characterizes the wrench induced on $\mathcal{B}$ by an individual contact under the Hertz-Walton compliance model. Let q_0 denote the object's equilibrium grasp configuration, which is assumed to be preloaded in accordance with the Hertz-Walton model. Denote by f_i the i^{th} contact force acting on $\mathcal{B}$ at x_i, described in a fixed reference frame. Denote by t_i and n_i the unit tangent and inward unit normal to $\mathcal{B}$ at x_i, and by $R_i(q_0) = [t_i\, n_i]$ the 2×2 orientation matrix of the i^{th} contact frame at q_0. The contact force f_i is given by

$$f_i = R_i(q_0)\begin{pmatrix} f_i^t \\ f_i^n \end{pmatrix},$$

where (f_i^t, f_i^n) are specified in terms of (δ_i^t, δ_i^n) by the Hertz-Walton model. The i^{th} *contact stiffness matrix*, denoted $K_i(q_0)$, is the 2×2 matrix representing the linearized force-displacement relationship at the i^{th} contact:

$$\begin{pmatrix} \Delta f_i^t \\ \Delta f_i^n \end{pmatrix} = K_i(q_0) \begin{pmatrix} \Delta \delta_i^t \\ \Delta \delta_i^n \end{pmatrix}, \tag{6}$$

where $K_i(q_0)$ is specified below. The matrix $K_i(q_0)$ induces a wrench-displacement relationship in $\mathcal{B}$'s c-space as follows. Let $\Delta q = q - q_0$ denote a small c-space displacement of $\mathcal{B}$ about q_0. Let $\Delta \boldsymbol{w}_i$ be the wrench generated by the i^{th} contact on $\mathcal{B}$ due to the displacement Δq. Using the notation $\boldsymbol{\delta}_i(q) = (\delta_i^t(q), \delta_i^n(q))$, the pair $(\Delta f_i^t, \Delta f_i^n)$ is related to Δq by

$$\begin{pmatrix} \Delta f_i^t \\ \Delta f_i^n \end{pmatrix} = K_i(q_0) D\boldsymbol{\delta}_i(q_0) \Delta q, \tag{7}$$

where $D\boldsymbol{\delta}_i$ is the 2×3 Jacobian of $\boldsymbol{\delta}_i(q)$ with respect to q. The wrench induced by $(\Delta f_i^t, \Delta f_i^n)$ on $\mathcal{B}$ is given by $\Delta \boldsymbol{w}_i = G_i^T R_i \left(\begin{smallmatrix} \Delta f_i^t \\ \Delta f_i^n \end{smallmatrix} \right)$, where $G_i = DX_{r_i}$ is the 2×3 Jacobian of X_{r_i}. Multiplying both sides of (7) by $G_i^T R_i$ gives the c-space relation:

$$\Delta \boldsymbol{w}_i = \left[G_i^T(q_0) R_i(q_0) K_i(q_0) D\boldsymbol{\delta}_i(q_0) \right] \Delta q = \tilde{K}_i(q_0) \Delta q.$$

The 3×3 matrix $\tilde{K}_i(q_0)$ is the i^{th} *contact c-space stiffness matrix.* It represents the linearized wrench-displacement relationship induced on $\mathcal{B}$ by the i^{th} contact.

We now derive formulas for the i^{th} contact stiffness matrix, $K_i(q_0)$, based on the Hertz-Walton model. Walton's law assumes a linear loading profile. It is therefore valid only for small changes $(\Delta \delta_i^t, \Delta \delta_i^n)$ aligned with the nominal loading profile. On the other hand, $K_i(q_0)$ gives the contact reaction force in response to arbitrary small displacements $(\Delta \delta_i^t, \Delta \delta_i^n)$. To obtain a formula for $K_i(q_0)$, we introduce the practical assumption that *closely matching*

loading profiles generate closely matching tangential traction fields.[3] This practical assumption is supported by the experiments described in Section 6. Under this assumption the tangential traction field resulting from a linear loading followed by arbitrary small displacements can be obtained from the Hertz-Walton model. The formulas for $K_i(q_0)$ and $\tilde{K}_i(q_0)$ are as follows.

Lemma 3.1. *Let two quasi-rigid bodies $\mathcal{A}_i$ and $\mathcal{B}$ with spherical tips of radii $r_{\mathcal{A}_i}$ and $r_{\mathcal{B}_i}$ be preloaded along a linear profile $\delta_i^t(q) = c_i\delta_i^n(q)$ such that $|c_i| < \mu\frac{(2-\nu)}{2(1-\nu)}$. The i^{th} contact stiffness matrix under the Hertz-Walton law is the 2×2 matrix:*

$$K_i(q_0) = 4G\sqrt{r_i}\sqrt{\delta_i^n(q_0)}\begin{bmatrix} -\frac{4}{3(2-\nu)} & -\frac{2c_i}{3(2-\nu)} \\ 0 & \frac{1}{1-\nu} \end{bmatrix}, \tag{8}$$

where $\delta_i^n(q_0)$ is the normal penetration, $r_i = r_{\mathcal{A}_i}r_{\mathcal{B}_i}/(r_{\mathcal{A}_i}+r_{\mathcal{B}_i})$, and G and ν are the material shear modulus and Poisson ratio. The c-space stiffness matrix induced by $K_i(q_0)$ is the 3×3 matrix:

$$\tilde{K}_i(q_0) = -4G\sqrt{r_i}\sqrt{\delta_i^n(q_0)}G_i^T(q_0)R_i(q_0)\begin{bmatrix} \frac{4}{3(2-\nu)} & -\frac{2c_i}{3(2-\nu)} \\ 0 & \frac{1}{1-\nu} \end{bmatrix}R_i^T(q_0)G_i(q_0), \tag{9}$$

where $R_i = [t_i\, n_i]$ and $G_i = DX_{r_i}$.

Note that $K_i(q_0)$ and consequently $\tilde{K}_i(q_0)$ are *asymmetric* matrices. The implication of this asymmetry on the stiffness and stability of multi-contact grasps is investigated in Section 4.

Proof: The formula for $K_i(q_0)$ is obtained by taking the derivative of (f_i^t, f_i^n) given in (2) and (5) with respect to (δ_i^t, δ_i^n), then substituting the loading path relation $\delta_i^t(q_0) = c_i\delta_i^n(q_0)$. Next consider the 3×3 matrix $\tilde{K}_i(q_0) = G_i^T(q_0)R_i(q_0)K_i(q_0)D\boldsymbol{\delta}_i(q_0)$. Since $\boldsymbol{\delta}_i = (\delta_i^t, \delta_i^n)$, the rows of the 2×3 Jacobian $D\boldsymbol{\delta}_i(q_0)$ are the differentials $D\delta_i^t(q_0)$ and $D\delta_i^n(q_0)$. Since $\frac{d}{dt}\delta_i^t(q(t)) = t_i\cdot G_i(q(t))\dot{q}$ according to (3), $D\delta_i^t = t_i^T G_i$. Similarly, it can be verified that $\frac{d}{dt}\delta_i^n(q(t)) = -n_i\cdot G_i(q(t))\dot{q}$ [32], and consequently $D\delta_i^n = -n_i^T G_i$.[4] The formula for $D\boldsymbol{\delta}_i(q_0)$ is thus $D\boldsymbol{\delta}_i(q_0) = \begin{bmatrix} t_i^T \\ -n_i^T \end{bmatrix}G_i(q_0)$. Substituting for $K_i(q_0)$ and $D\boldsymbol{\delta}_i(q_0)$ in the product

[3] The distance between the two loading paths can be measured with a metric such as $d(\alpha(t),\beta(t)) = \max_{t_0\le t\le t_1}|\alpha(t)-\beta(t)|$, where $\alpha(t)$ and $\beta(t)$ parametrize the two loading paths for $t\in[t_0,t_1]$.

[4] The contact normal n_i points into $\mathcal{B}$. Substituting $\dot{x}_i = G_i\dot{q}$, $\frac{d}{dt}\delta_i^n(q(t)) = (-n_i)\cdot\dot{x}_i > 0$ when $\mathcal{B}$ penetrates deeper into $\mathcal{A}_i$, while the converse holds when $\frac{d}{dt}\delta_i^n(q(t)) < 0$.

$K_i(q_0)D\boldsymbol{\delta}_i(q_0)$ gives

$$\begin{aligned} K_i(q_0)D\boldsymbol{\delta}_i(q_0) &= \begin{bmatrix} -\frac{4}{3(2-\nu)} & -\frac{2c_i}{3(2-\nu)} \\ 0 & \frac{1}{1-\nu} \end{bmatrix} \begin{bmatrix} t_i^T \\ -n_i^T \end{bmatrix} G_i(q_0) \\ &= -\begin{bmatrix} \frac{4}{3(2-\nu)} & -\frac{2c_i}{3(2-\nu)} \\ 0 & \frac{1}{1-\nu} \end{bmatrix} \begin{bmatrix} t_i^T \\ n_i^T \end{bmatrix} G_i(q_0) \\ &= -\begin{bmatrix} \frac{4}{3(2-\nu)} & -\frac{2c_i}{3(2-\nu)} \\ 0 & \frac{1}{1-\nu} \end{bmatrix} R_i^T(q_0) G_i(q_0), \end{aligned}$$

where we omitted the scalars preceding $K_i(q_0)$ and substituted $R_i^T = \begin{bmatrix} t_i^T \\ n_i^T \end{bmatrix}$. Pre-multiplying the latter expression by $G_i^T(q_0)R_i(q_0)$ gives the formula for $\tilde{K}_i(q_0)$. □

In preparation for the grasp stability analysis conducted in Section 4, we establish when the symmetric part of $\tilde{K}_i$, $(\tilde{K}_i)_s = \frac{1}{2}\big(\tilde{K}_i + \tilde{K}_i^T\big)$, is negative semi-definite. A key result is that the negative semi-definiteness of $(\tilde{K}_i)_s$ depends solely on the slope of the linear loading profile.

Proposition 3.2. *Let the i^{th} contact be loaded along a linear loading profile with slope c_i. If the loading profile satisfies the inequality*

$$|c_i| < 2\sqrt{\frac{3(2-\nu)}{(1-\nu)}}, \tag{10}$$

the symmetrized i^{th} contact c-space stiffness matrix, $\big(\tilde{K}_i(q_0)\big)_s$, is **negative semi-definite.**

Proof: Denote by A_i the 2×2 matrix at the core of $\tilde{K}_i(q_0)$ in (9):

$$A_i = \begin{bmatrix} \frac{4}{3(2-\nu)} & -\frac{2c_i}{3(2-\nu)} \\ 0 & \frac{1}{1-\nu} \end{bmatrix}.$$

Then $(\tilde{K}_i)_s = -G_i^T R_i (A_i)_s R_i^T G_i$, where we omitted the positive scalars preceding $\tilde{K}_i$. The positive definiteness of $(A_i)_s$ implies the negative semi-definiteness of $(\tilde{K}_i)_s$. The 2×2 matrix $(A_i)_s$ is positive definite when its two eigenvalues, λ_1 and λ_2, are strictly positive. First consider the trace of $(A_i)_s$, $\mathsf{tr}(A_i)_s = \lambda_1 + \lambda_2$. Inspection of the diagonal elements in $(A_i)_s$ reveals that $\mathsf{tr}(A_i)_s > 0$ when $\nu < 1$. Since Poisson's ratio satisfies $0 \leq \nu \leq 0.5$ for all practical materials, $\mathsf{tr}(A_i)_s > 0$. Next consider the determinant of $(A_i)_s$, $\det(A_i)_s = \lambda_1\lambda_2$. Since $\lambda_1 + \lambda_2 > 0$, a positive determinant would imply positive definiteness of $(A_i)_s$. The determinant of $(A_i)_s$ is:

$$\det(A_i)_s = \frac{4}{3(1-\nu)(2-\nu)} - \frac{c_i^2}{9(2-\nu)^2}.$$

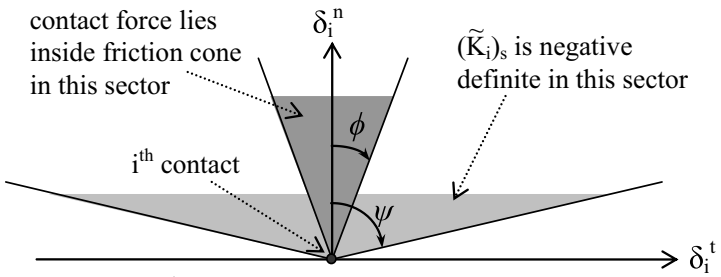

Figure 3: The sectors in the (δ_i^t, δ_i^n)-plane associated with a negative semi-definite $(\tilde{K}_i)_s$ and the friction cone constraint. Typically $|\phi| < 45°$ while $|\psi| < 78.5°$.

The inequality $\det(A_i)_s > 0$ becomes $4/(1-\nu) > c_i^2/3(2-\nu)$. A square root of both sides gives the condition for the positive definiteness of $(A_i)_s$, which implies the negative semi-definiteness of $(\tilde{K}_i)_s$. □

Example: Consider the constraint imposed on the linear loading slope by condition (10). Since $0 \leq \nu \leq 0.5$, the term $(2-\nu)/(1-\nu)$ varies in the interval $[2, 3]$. Hence $(\tilde{K}_i)_s$ is negative semi-definite when $|c_i| < 2\sqrt{6}$. The corresponding slope angle of the linear loading profile, denoted ψ in Figure 3, must satisfy $|\psi| < 78.5°$. The slope of the linear loading profile must also satisfy the friction cone constraint specified in (5), $|c_i| < \mu(2-\nu)/2(1-\nu)$. Since $(2-\nu)/2(1-\nu)$ varies in the interval $[1, 3/2]$, the friction cone constraint is satisfied when $|c_i| < \mu$. The linear loading path must always satisfy the friction cone constrain. The negative semi-definiteness of $(\tilde{K}_i)_s$ is therefore automatic as long as $\mu \leq 2\sqrt{6}$, which clearly holds in most practical situations.[5] For instance, when $\mu = 1$ the linear loading slope angle, denoted ϕ in Figure 3, must satisfy $|\phi| < 45°$, which is well within the 78.5° constraint imposed by (10). The symmetrized matrix $(\tilde{K}_i)_s$ is thus negative semi-definite in typical linearly loaded grasps.

4 Grasp Stiffness and Stability Analysis

Based on the wrench-displacement relationship affected at the individual contacts by the Hertz-Walton compliance model, this section characterizes the stiffness and stability of multi-contact grasps. Section 4.1 derives the linearized dynamics of $\mathcal{B}$ at a multi-contact equilibrium grasp. The resulting grasp dynamics is governed by an asymmetric grasp stiffness matrix. Section 4.2 introduces a generic stability criterion for asymmetric linear systems [34], then applies the criterion to obtain the conditions under which $\mathcal{B}$ is stably held by the compliant contacts.

[5] For larger μ, the negative semi-definiteness of $(\tilde{K}_i)_s$ is automatic in the sector $|c_i| < 2\sqrt{6}$. The stability of grasps loaded with other linear paths can be evaluated numerically using tools developed in Section 4.

4.1 Linearized Grasp Dynamics

Consider an object $\mathcal{B}$ held in equilibrium grasp by stationary finger bodies $\mathcal{A}_1, \ldots, \mathcal{A}_k$. The bodies are assumed to lie on a frictionless horizontal plane, such that the inter-body forces are parallel to the supporting plane. The undeformed bodies are assumed to have spherical surfaces at the contacts, and the contacts are assumed to be preloaded along linear loading profiles in accordance with the Hertz-Walton model. The wrench induced on $\mathcal{B}$ by a contact force f_i acting at x_i is given by $G_i^T f_i$, where $G_i = DX_{r_i}$ is the Jacobian of $X_{r_i}(q)$. The dynamics of $\mathcal{B}$ within the planar environment under the influence of k contact forces, without any other external influences such as gravity, is given by

$$M(q)\ddot{q} + C(q,\dot{q}) = \sum_{i=1}^{k} G_i^T(q) f_i(q,\dot{q}), \tag{11}$$

where $M(q)$ is $\mathcal{B}$'s 3×3 inertia matrix, and $C(q,\dot{q})$ is the vector of centrifugal and Coriolis forces acting on $\mathcal{B}$. As before, q_0 denotes the object's equilibrium configuration. To determine the linearized dynamics of $\mathcal{B}$ at $(q,\dot{q}) = (q_0, 0)$, denote by $(p_1, p_2) = (q, \dot{q})$ the object's state variables. Then (11) can be written as

$$\begin{array}{l} \dot{p}_1 = p_2 \\ \dot{p}_2 = M^{-1}(p_1)\big(\sum_{i=1}^{k} G_i^T(p_1) f_i(p_1,p_2) - C(p_1,p_2)\big). \end{array} \tag{12}$$

The following proposition describes the linearized dynamics of $\mathcal{B}$ at $(q_0, 0)$ (see appendix for a proof of the proposition).

Proposition 4.1. *Let a quasi-rigid body $\mathcal{B}$ be held at an equilibrium grasp configuration, $q_0 = (d_0, \theta_0)$, by quasi-rigid finger bodies $\mathcal{A}_1, \ldots, \mathcal{A}_k$, without external influences such as gravity. Let $\Delta p_1 = q - q_0$ and $\Delta p_2 = \dot{q} - 0$. The* **linearized dynamics** *of $\mathcal{B}$ at $(q_0, 0)$ is given by*

$$\frac{d}{dt}\begin{pmatrix}\Delta p_1 \\ \Delta p_2\end{pmatrix} = \begin{bmatrix} O_{3\times 3} & I_{3\times 3} \\ -M^{-1}(q_0)K_p(q_0,0) & -M^{-1}(q_0)K_d(q_0,0)\end{bmatrix}\begin{pmatrix}\Delta p_1 \\ \Delta p_2\end{pmatrix}, \tag{13}$$

where K_p and K_d are the grasp stiffness and damping matrices. The grasp **stiffness matrix** *is the asymmetric 3×3 matrix:*

$$K_p(q_0,0) = -\sum_{i=1}^{k}\left\{\tilde{K}_i(q_0) - \begin{bmatrix} O_{2\times 2} & 0 \\ 0^T & \boldsymbol{\rho}_i(\theta_0)\cdot f_i \end{bmatrix} + G_i^T(q_0)\begin{bmatrix} f_i^n & f_i^t \\ -f_i^t & f_i^n \end{bmatrix} Dn_i(q_0)\right\}, \tag{14}$$

where $\tilde{K}_i(q_0)$ is the i^{th} contact c-space stiffness matrix, $\boldsymbol{\rho}_i(\theta_0)$ is the i^{th} contact position relative to $\mathcal{B}$'s origin, f_i is the i^{th} contact force with components (f_i^t, f_i^n), and n_i is the i^{th}

contact normal $(i = 1 \dots k)$. *The grasp* **damping matrix** *is the symmetric* 3×3 *matrix:*

$$K_d(q_0, 0) = \sum_{i=1}^{k} \delta_i^n(q_0) G_i^T(q_0) R_i(q_0) \begin{bmatrix} \frac{\partial \varphi_i^t}{\partial \dot{\delta}_i^t}(0) & 0 \\ 0 & \frac{\partial \varphi_i^n}{\partial \dot{\delta}_i^n}(0) \end{bmatrix} R_i^T(q_0) G_i(q_0), \tag{15}$$

where φ_i^t *and* φ_i^n *are the* i^{th} *tangential and normal damping functions evaluated at* $\dot{\delta}_i^t = \dot{\delta}_i^n = 0$ $(i = 1 \dots k)$.

Let us discuss the three terms appearing in the stiffness matrix K_p. The first term, $-\sum_{i=1}^{k} \tilde{K}_i$, represents the net wrench affected by the compliant contacts on $\mathcal{B}$. This term is an *asymmetric* matrix under the Hertz-Walton compliance model. As a result, the linearized grasp dynamics is *not* governed by any potential energy function. The second term, $\sum_{i=1}^{k} \boldsymbol{\rho}_i \cdot f_i$, represents the effect of the preload forces on the grasp stiffness matrix. When the preload level is too high this term can possibly destabilize the grasp, a phenomena known as "coin snapping" in the grasping literature [6, 23, 28]. The third term represents the overlap-segment change of direction due to small displacements of $\mathcal{B}$. This term depends on the radii of curvature of the undeformed bodies. As shown in Ref. [23], the 2×3 Jacobian Dn_i is given by

$$Dn_i(q_0) = \frac{1}{r_{\mathcal{A}_i} + r_{\mathcal{B}_i} - \delta_i^n(q_0)} \left[I - n_i n_i^T, \ (r_{\mathcal{B}_i} + \boldsymbol{\rho}_i(\theta_0) \cdot n_i) J n_i \right], \tag{16}$$

where I is a 2×2 identity matrix, $J = \begin{bmatrix} 0 & -1 \\ 1 & 0 \end{bmatrix}$, and $r_{\mathcal{A}_i}$ and $r_{\mathcal{B}_i}$ are the radii of curvature of $\mathcal{A}_i$ and $\mathcal{B}$ at the endpoints of the i^{th} overlap segment. The curvature term in K_p also depends on the preload force components, (f_i^t, f_i^n) for $i = 1 \dots k$. Therefore when curvature effects have a stabilizing influence, their influence becomes more pronounced with higher preload levels (see Section 5). Finally, the damping matrix, K_d, is proportional to the normal penetration, δ_i^n, which is strictly positive at the preloaded contacts. Since the damping functions φ_i^t and φ_i^n are monotonically increasing in their arguments, K_d is positive semi-definite. It is strictly positive definite when the object and finger bodies lie on a supporting plane, since any instantaneous planar motion of $\mathcal{B}$ incurs strict damping at one of the contacts.

We will analyze the equilibrium grasp stability based on a generic stability criterion for asymmetric second-order linear systems. To apply this criterion, write the linearized grasp dynamics (13) in the standard form:

$$M(q_0) \Delta \ddot{q} + K_d(q_0, 0) \Delta \dot{q} + K_p(q_0, 0) \Delta q = \vec{0}, \tag{17}$$

where $\Delta q = q - q_0$ and $\Delta \dot{q} = \dot{q} - 0$. Note that $M(q_0)$ and $K_d(q_0, 0)$ are symmetric positive definite matrices while $K_p(q_0, 0)$ is an asymmetric matrix.

4.2 Stability of Second-Order Asymmetric Linear Systems

The local stability of a compliant equilibrium grasp can be generically determined from its linearized dynamics at the equilibrium grasp. When the contacts are governed by the Hertz-Walton compliance law, the linearized grasp dynamics forms an asymmetric second-order linear system (Proposition 4.1). The stability of such systems can be determined as follows. Given an $n \times n$ matrix A, its symmetric and asymmetric parts are given by $A_s = \frac{1}{2}(A + A^T)$ and $A_{as} = \frac{1}{2}(A - A^T)$. Its norm is given by $\|A\| = \max_{\|v\| \leq 1}\{\|Av\|\}$ for $v \in \mathbb{R}^n$. When A is a symmetric matrix its minimal eigenvalue is denoted $\lambda_{min}(A)$.

The following theorem describes a generic criterion for the stability of asymmetric second-order linear systems.

Theorem 1 ([34]). *Consider the second-order linear system in the variable $p \in \mathbb{R}^n$,*

$$M\ddot{p} + K_d\dot{p} + K_p p = \vec{0}, \tag{18}$$

where $M \in \mathbb{R}^{n\times n}$ and $K_d \in \mathbb{R}^{n\times n}$ are symmetric positive definite matrices, while $K_p \in \mathbb{R}^{n\times n}$ is an asymmetric matrix such that $(K_p)_s$ is positive definite. Let $\alpha > 0$ be the minimal eigenvalue of $M^{-1/2}(K_p)_s M^{-1/2}$, let $\beta > 0$ be the minimal eigenvalue of $M^{-1/2}K_d M^{-1/2}$, and let $\gamma \geq 0$ be the matrix norm of $M^{-1/2}(K_p)_{as}M^{-1/2}$. If α, β, and γ satisfy the relation:

$$\gamma < \sqrt{\alpha}\beta \tag{19}$$

the linear system (18) is **globally asymptotically stable.**

The condition $\gamma < \sqrt{\alpha}\beta$ can be interpreted as follows. Consider the case where M is an identity matrix. Then $\alpha = \lambda_{min}\big((K_p)_s\big)$, $\beta = \lambda_{min}(K_d)$, and the condition $\gamma < \sqrt{\alpha}\beta$ becomes:

$$\|(K_p)_{as}\| < \lambda_{min}(K_d)\sqrt{\lambda_{min}\big((K_p)_s\big)}.$$

The stability condition essentially requires that the asymmetric part of K_p be sufficiently small relative to the symmetric part of K_p (which is modulated by the damping $\lambda_{min}(K_d)$).

The following key theorem applies the generic stability criterion, $\gamma < \sqrt{\alpha}\beta$, to the linearized grasp dynamics.

Theorem 2 (**Compliant Grasp Stability**). *Let a quasi-rigid body $\mathcal{B}$ be held at an equilibrium grasp q_0 by quasi-rigid bodies $\mathcal{A}_1, \ldots, \mathcal{A}_k$ satisfying the Hertz-Walton compliance law. Define the scalars α, β, and γ as*

$$\begin{aligned}
\alpha &= \lambda_{min}\left(M^{-\frac{1}{2}}(q_0)(K_p(q_0,0))_s M^{-\frac{1}{2}}(q_0)\right)\\
\beta &= \lambda_{min}\left(M^{-\frac{1}{2}}(q_0)K_d(q_0,0)M^{-\frac{1}{2}}(q_0)\right)\\
\gamma &= \|M^{-\frac{1}{2}}(q_0)(K_p(q_0,0))_{as}M^{-\frac{1}{2}}(q_0)\|,
\end{aligned}$$

where $M(q_0)$ is $\mathcal{B}$'s inertia matrix, $K_p(q_0,0)$ is the grasp stiffness matrix, and $K_d(q_0,0)$ is the grasp damping matrix.
If $\alpha > 0$, $\beta > 0$, and $\gamma < \sqrt{\alpha}\beta$, the zero-velocity state $(q_0,0)$ of the nonlinear grasp dynamics (11) is **locally asymptotically stable.**

Proof: A nonlinear system $\dot{x} = F(x)$ has a *hyperbolic* equilibrium at x_0 when $F(x_0) = \vec{0}$ and the Jacobian $DF(x_0)$ has eigenvalues with non-zero real part [15]. When the system $\dot{x} = F(x)$ has a hyperbolic equilibrium at x_0, its local stability is fully determined by the system's linearized dynamics at x_0 according to the Hartman-Grobman lemma [13]. The linearized grasp dynamics at $(q_0,0)$ has the form (see eq. (17)):

$$M(q_0)\Delta\ddot{q} + K_d(q_0)\Delta\dot{q} + K_p(q_0)\Delta q = 0. \tag{20}$$

Based on Theorem 1, the conditions $\alpha > 0$, $\beta > 0$, and $\gamma < \sqrt{\alpha}\beta$, ensure the global asymptotically stability of the linear system (20). The asymptotically stable equilibrium of the linearized system is necessarily a hyperbolic equilibrium of the nonlinear system. The nonlinear grasp dynamics is therefore locally asymptotically stable. □

Remark: The model specified in (1) for the compliant normal force component, f_i^n, is valid as long as the net normal force remains strictly positive. This requirement holds in a small neighborhood of $(q_0,0)$ for the following reason. Substituting $f_i^n = g_i(\delta_i^n) + \delta_i^n \cdot \varphi_i^n(\dot{\delta}_i^n)$ according to (1), the model is valid in the set:

$$\mathcal{U} = \{(q,\dot{q}) : g_i(\delta_i^n(q)) + \delta_i^n(q) \cdot \varphi_i^n(\dot{\delta}_i^n(q,\dot{q})) > 0 \quad \text{for} \quad i = 1 \ldots k\}.$$

At the equilibrium grasp $\delta_i^n(q_0) > 0$ and $\dot{\delta}_i^n(q_0,0) = 0$ for $i = 1 \ldots k$. Therefore $\mathcal{U}$ contains the point $(q_0,0)$ in its interior. The Hartman-Grobman lemma ensures that $(q_0,0)$ is surrounded by two neighborhoods. An outer neighborhood $\mathcal{V}$ and a smaller neighborhood $\mathcal{V}' \subseteq \mathcal{V}$, such that every trajectory that starts in $\mathcal{V}'$ at $t = 0$ converges to $(q_0,0)$ while remaining in $\mathcal{V}$ for $t \geq 0$. The Hartman-Grobman lemma is established via the construction of a local Lyapunov function at $(q_0,0)$ [13]. This function can be used to ensure that a sufficiently small neighborhood $\mathcal{V}$ lies inside $\mathcal{U}$. All trajectories that start in the smaller neighborhood, $\mathcal{V}' \subseteq \mathcal{V}$, converge to $(q_0,0)$ while remaining within $\mathcal{U}$ for $t \geq 0$. The equilibrium $(q_0,0)$ is thus locally asymptotically stable under the normal compliance model.

5 Synthesis of Compliantly Stable Grasps

This section suggests practical guidelines for synthesizing compliantly stable grasps based on the stability criterion of Theorem 2. To synthesize a stable grasp, one must satisfy the three

conditions $\alpha > 0$, $\beta > 0$, and $\gamma < \sqrt{\alpha}\beta$. To simplify the discussion, assume the object $\mathcal{B}$ is grasped along *planar facets* perpendicular to the supporting plane. In this case the grasp stiffness matrix, K_p, has the following simple form (see appendix for a proof of the lemma).

Lemma 5.1. *When $\mathcal{B}$ is held in equilibrium grasp along planar facets, the grasp stiffness matrix specified in eq. (14) becomes*

$$K_p(q_0, 0) = -\sum_{i=1}^{k} \tilde{K}_i(q_0), \tag{21}$$

where $\tilde{K}_i(q_0)$ is the i^{th} c-space contact stiffness matrix ($i = 1 \dots k$).

As shown in the proof of the lemma, when $\mathcal{B}$ is held along planar facets curvature effects contribute a stabilizing term to K_p. (This stabilizing effect can be intuitively observed by holding a coin along its flat facets with two fingers; the coin remains stably held by the two fingers even when the preload forces increase.) The stabilizing curvature term cancels the term proportional to the preload forces in (14), and the resulting K_p depends solely on the contact stiffness matrices, $K_p = -\sum_{i=1}^{k} \tilde{K}_i$.

The $\alpha > 0$ condition: Since $\alpha = \lambda_{min}(M^{-1/2}(K_p)_s M^{-1/2})$ and $M^{-1/2}$ is non-singular, the condition $\alpha > 0$ is equivalent to the condition $\lambda_{min}\big((K_p)_s\big) > 0$. The symmetric part of K_p is given by

$$(K_p(q_0, 0))_s = -\sum_{i=1}^{k} \big(\tilde{K}_i(q_0)\big)_s.$$

According to Proposition 3.2, each $(\tilde{K}_i)_s$ is negative semi-definite when the slope of the i^{th} linear loading profile, c_i, satisfies a mild requirement which is automatically maintained for friction coefficients in the range $\mu \leq 2\sqrt{6}$. For these friction coefficients $(K_p)_s$ is positive definite based on the following argument. According to Lemma 3.1, each $(\tilde{K}_i)_s$ is given by

$$\big(\tilde{K}_i(q_0)\big)_s = -\sqrt{\delta_i^n(q_0)} G_i^T(q_0) R_i(q_0) \begin{bmatrix} \frac{4}{3(2-\nu)} & -\frac{2c_i}{3(2-\nu)} \\ 0 & \frac{1}{1-\nu} \end{bmatrix}_s R_i^T(q_0) G_i(q_0), \tag{22}$$

where we omitted the positive scalars $4G\sqrt{r_i}$. The matrix $(\tilde{K}_i(q_0))_s$ has a one-dimensional kernel. Since $G_i(q_0) = DX_{r_i}$, the kernel of $(\tilde{K}_i(q_0))_s$ occurs along instantaneous motions of $\mathcal{B}$ satisfying $DX_{r_i}\dot{q} = \dot{x}_i = \vec{0}$, where $\dot{x}_i$ is the i^{th} contact point velocity. Such motions correspond to instantaneous rolling of $\mathcal{B}$ about x_i. Since $\mathcal{B}$ cannot instantaneously roll about $k \geq 2$ contacts in $2D$, the matrix $(K_p)_s = -\sum_{i=1}^{k} (\tilde{K}_i)_s$ is positive definite (and hence $\alpha > 0$) for reasonable friction coefficients.

The $\beta > 0$ condition: Since $\beta = \lambda_{min}(M^{-1/2} K_d M^{-1/2})$ and $M^{-1/2}$ is non-singular, the condition $\beta > 0$ is equivalent to the condition $\lambda_{min}(K_d) > 0$. The damping matrix is given by

$$K_d(q_0, 0) = \sum_{i=1}^{k} \delta_i^n(q_0) G_i^T(q_0) R_i(q_0) \begin{bmatrix} \frac{\partial \varphi_i^t}{\partial \dot{\delta}_i^t}(0) & 0 \\ 0 & \frac{\partial \varphi_i^n}{\partial \dot{\delta}_i^n}(0) \end{bmatrix} R_i^T(q_0) G_i(q_0).$$

The damping functions $\varphi_i^t(\dot{\delta}_i^t)$ and $\varphi_i^n(\dot{\delta}_i^n)$ are monotonically increasing in their arguments. Hence $\frac{\partial \varphi_i^t}{\partial \dot{\delta}_i^t}(0)$ and $\frac{\partial \varphi_i^n}{\partial \dot{\delta}_i^n}(0)$ are strictly positive. Since $\delta_i^n(q_0) > 0$ for $i = 1 \ldots k$ and $\mathcal{B}$ cannot instantaneously roll about all k contacts, the matrix K_d is positive definite and hence $\beta > 0$.

While K_d is positive definite, its exact value depends on intricate damping processes. For instance, small movements of $\mathcal{B}$ induce frictional micro-slip within the contact regions. Damping is also induced by viscoelastic effects within the compressed material (e.g. [11][177-182],[20][242-247],[38][26-31]). The modeling of damping in compliant grasps is under investigation by several research groups [40, 41, 42]. Until such models become available, we lump the net effect of damping by a positive scalar, $\kappa_d = \lambda_{min}(M^{-1/2} K_d M^{-1/2}) > 0$.

The $\gamma < \sqrt{\alpha}\beta$ condition: Since $\alpha = \lambda_{min}\big((K_p)_s\big)$ and $\gamma = \|M^{-1/2}(K_p)_{as} M^{-1/2}\|$, the condition $\gamma < \sqrt{\alpha}\beta$ is given by

$$\|M^{-\frac{1}{2}}\big(K_p(q_0, 0)\big)_{as} M^{-\frac{1}{2}}\| < \kappa_d \sqrt{\lambda_{min}(M^{-\frac{1}{2}}\big(K_p(q_0, 0)\big)_s M^{-\frac{1}{2}})}. \tag{23}$$

It is now shown that (23) limits the allowed linear loading profiles to particular sectors centered on the contact normals. Let us first scale the c-space coordinates by the grasp's characteristic length (this scaling essentially normalizes $\mathcal{B}$'s orientation coordinate relative to its translation coordinates). Define the *grasp centroid* to be the average contact position: $x_c = \frac{1}{k} \sum_{i=1}^{k} x_i$, where $x_1, \ldots, x_k$ are the contact locations. The grasp's *characteristic length* is the mean squared distance of the contacts from x_c:

$$l_c = \sqrt{\frac{1}{k} \sum_{i=1}^{k} \|x_i - x_c\|^2}.$$

The parameter l_c induces the following scaling of $\mathcal{B}$'s c-space coordinates

$$q = S\bar{q} \quad \text{where} \quad S = \begin{bmatrix} I_{2\times 2} & 0 \\ 0^T & 1/l_c \end{bmatrix}.$$

The grasp's stiffness matrix and $\mathcal{B}$'s inertia matrix are given in the $\bar{q}$ coordinates by

$$\bar{K}_p(\bar{q}_0, 0) = S^T K_p(q_0, 0) S \quad \text{and} \quad \bar{M}(\bar{q}_0) = S^T M(q_0) S \qquad \text{where } q_0 = S\bar{q}_0.$$

Condition (23) is specified in the $\bar{q}$ coordinates by

$$\|\bar{M}^{-\frac{1}{2}}\big(\bar{K}_p(\bar{q}_0,0)\big)_{as}\bar{M}^{-\frac{1}{2}}\| < \kappa_d\sqrt{\lambda_{min}(\bar{M}^{-\frac{1}{2}}\big(\bar{K}_p(\bar{q}_0,0)\big)_s\bar{M}^{-\frac{1}{2}})}. \tag{24}$$

In order to proceed with the assessment of (24), let us approximate the normal penetration at the contacts, $\delta_i^n(q_0)$ for $i=1\dots k$, by a characteristic normal penetration, $\delta_c^n \cong \delta_i^n(q_0)$ for $i=1\dots k$. Let us also approximate the loading profile slopes, c_i for $i=1\dots k$, by a characteristic slope parameter, $c\cong c_i$ for $i=1\dots k$. When these approximations are substituted into the matrices $\tilde{K}_i$ for $i=1\dots k$, the symmetric and asymmetric parts of $\bar{K}_p = -\sum_{i=1}^k S^T\tilde{K}_i S$ are given by

$$\big(\bar{K}_p(\bar{q}_0,0)\big)_s \cong \sqrt{\delta_c^n}\sum_{i=1}^k S^T G_i^T R_i A_s R_i^T G_i S \tag{25}$$

and

$$\big(\bar{K}_p(\bar{q}_0,0)\big)_{as} \cong \sqrt{\delta_c^n}\sum_{i=1}^k S^T G_i^T R_i A_{as} R_i^T G_i S, \tag{26}$$

where A_s and A_{as} are the symmetric and asymmetric parts of the 2×2 matrix:

$$A = \begin{bmatrix} \frac{4}{3(2-\nu)} & -\frac{2c}{3(2-\nu)} \\ 0 & \frac{1}{1-\nu} \end{bmatrix}. \tag{27}$$

The matrix A represents the 2×2 contact stiffness matrices, where c is the characteristic slope of the linear loading profiles. The following proposition asserts that the condition $\gamma<\sqrt{\alpha}\beta$ essentially requires that A_{as} be sufficiently small relative to A_s (see appendix for a proof of the proposition).

Proposition 5.2. *Let $\mathcal{B}$ be held along planar facets in a k-finger grasp, such that $\delta_i^n(q_0)\cong\delta_c^n$ and $c_i\cong c$ for $i=1\dots k$. Let $\alpha>0$ and $\beta>0$ for the given grasp. The stability condition $\gamma<\sqrt{\alpha}\beta$ is satisfied when A_s and A_{as} satisfy the condition:*

$$\|A_{as}\| < \kappa_d\frac{\lambda_{min}(\bar{M})}{\lambda_{max}(\bar{M})}\sqrt{\lambda_{min}(A_s)}, \tag{28}$$

where A is specified in (27), κ_d is the damping parameter, and $\bar{M}$ is $\mathcal{B}$'s scaled inertia matrix.

Based on condition (28), one can determine the stable linear loading slopes as follows. The symmetric and asymmetric parts of A are given by

$$A_s = \begin{bmatrix} a(\nu) & -\frac{c}{3(2-\nu)} \\ -\frac{c}{3(2-\nu)} & b(\nu) \end{bmatrix} \quad \text{and} \quad A_{as} = \begin{bmatrix} 0 & -\frac{c}{3(2-\nu)} \\ \frac{c}{3(2-\nu)} & 0 \end{bmatrix},$$

where c is the characteristic slope of the linear loading profiles, $a(\nu) = 4/3(2-\nu)$, and $b(\nu) = 1/1-\nu$. The norm of A_{as} is given by $\|A_{as}\| = |c|/3(2-\nu)$, while the minimal eigenvalue of A_s satisfies the inequality $\lambda_{min}(A_s) \geq \det(A_s)/\mathsf{tr}(A_s)$.[6] Substituting for $\det(A_s)$ and $\mathsf{tr}(A_s)$, condition (28) is implied by the stricter inequality:

$$\frac{|c|}{3(2-\nu)} < \kappa_d \frac{\lambda_{min}(\bar{M})}{\lambda_{max}(\bar{M})} \left(\frac{a(\nu)b(\nu) - \frac{c^2}{9(2-\nu)^2}}{a(\nu)+b(\nu)} \right)^{\frac{1}{2}}. \tag{29}$$

The square root in (29) is well defined since $\alpha = \lambda_{min}(A_s) > 0$. After some algebraic manipulation, (29) can be written as the following constraint on the characteristic slope c:

$$|c| < 3\kappa \left(\frac{a(\nu)b(\nu)}{a(\nu)+b(\nu)+\kappa^2} \right)^{\frac{1}{2}} (2-\nu) \qquad \text{where } \kappa = \kappa_d \frac{\lambda_{min}(\bar{M})}{\lambda_{max}(\bar{M})}. \tag{30}$$

To summarize, (30) was derived from the stability criterion of Theorem 2 under the assumptions of Proposition 5.2. Grasp stability is ensured when the linear loading profiles lie in the sector specified by (30).

One is thus lead to the following qualitative guidelines for ensuring grasp stability (the precise stability can be numerically evaluated with the formulas of Theorem 2). As the allowed sectors are centered on the contact normals (corresponding to $c = 0$), one should ideally select contact locations at which the equilibrium grasp can be preloaded along the contact normals. If such contact locations are infeasible, one should select contact locations at which the feasible linear loading profiles are *as close as possible* to the contact normal directions. If the contact locations are pre-determined by other task constraints, align the linear loading profiles *as close as possible* to the contact normals within the allowed friction cones, as these directions will maximize the grasp stability margin with respect to small errors in the loading profile directions. These qualitative considerations are next illustrated with examples. The examples are designed to show the effect of the loading slope on grasp stability, hence they only vary the angle between the linear loading profile and the surface normal at the contacts.

Example—a two-finger grasp of a wedge-like object: The wedge-like object $\mathcal{B}$ shown in Figure 4(a) is held along planar facet by two spherical fixturing elements in a frictional equilibrium grasp. The object and fixturing elements are assumed to be made of Aluminum. The object's length is 20 cm, its width at the contacts is 5 cm, and its thickness is 10 cm. The object's head angle, denoted ϕ, varies as a free parameter. The fixturing elements, or "fingers," are 4 cm diameter spheres. The friction coefficient is assumed sufficiently large so

[6] If $\lambda_1 \leq \lambda_2$ are the eigenvalues of A_s (both positive), $\det(A_s)/\mathsf{tr}(A_s) = \lambda_1\lambda_2/(\lambda_1+\lambda_2) \leq \lambda_1$.

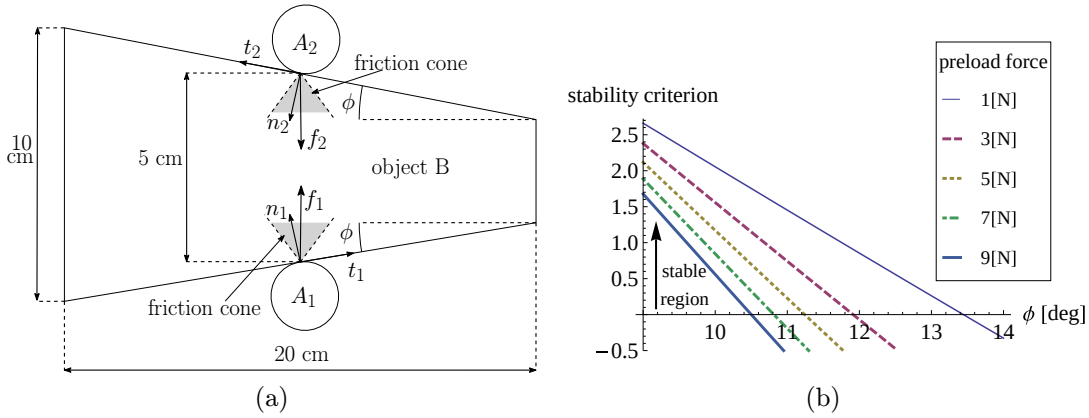

Figure 4: (a) A two-finger grasp of a parameterized wedge-like object. (b) The stability criterion, $\sqrt{\alpha}\beta-\gamma$, plotted as a function of $\mathcal{B}$'s head angle ϕ for several preload levels.

that the fingers do not slide. When the compliance of Aluminum is taken into account, the grasp stiffness matrix K_p is asymmetric and local deformations at the contacts may cause instability. When the finger preload forces, f_1 and f_2, are aligned with the contact normals, K_p is perfectly symmetric. However, equilibrium feasibility requires that the finger forces be collinear with opposite directions, thus enforcing oblique finger loading profiles. As the object's head angle ϕ increases, the finger forces must rotate away from the contact normal directions in order to maintain the equilibrium grasp. During this rotation $\|(K_p)_{as}\|$ increases from zero and the margin of stability specified in Proposition 5.2 becomes less favorable. The stability condition (28) limits the allowed finger force directions and consequently bounds the object's maximal allowed head angle (Figure 4(b)). As expected, higher preload forces decrease the maximal allowed head angle ϕ. For instance, at a preload level of 9 N, the stability criterion $\gamma < \sqrt{\alpha}\beta$ is maintained for head angles $0 \leq \phi \leq 10.5°$.

Example—a three-finger grasp of a wedge-like object: The same wedge-like object is next held by three fixturing elements, or "fingers," as shown in Figure 5(a). The finger $\mathcal{A}_1$ applies a vertical upward force, while the fingers $\mathcal{A}_2$ and $\mathcal{A}_3$ apply vertical downward forces. Note that the finger forces act at an oblique angle relative to the contact normals at the equilibrium grasp. Here, too, the finger forces rotate away from the contact normal directions as the object's head angle increases. Since $\|(K_p)_{as}\|$ increases during this rotation, the margin of stability becomes less favorable. The stability criterion, $\sqrt{\alpha}\beta-\gamma$, is monotonically decreasing in the object's head angle ϕ, thus limiting the range of allowed head angles under each preload level (Figure 5(b)). Note that the three-finger grasp admits a larger range of object head angles than the two-finger grasp. To explain this behavior, recall that

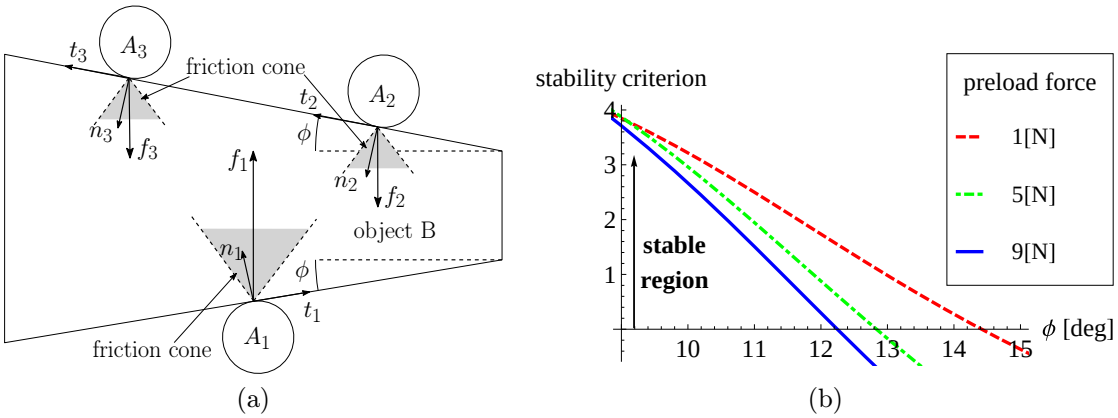

Figure 5: (a) A three-finger grasp of the same parametrized wedge-like object. (b) The stability criterion, $\sqrt{\alpha}\beta-\gamma$, plotted as a function of $\mathcal{B}$'s head angle ϕ for several preload levels.

when M is replaced by the identity matrix, the stability condition $\gamma < \sqrt{\alpha}\beta$ can be written as $\|(K_p)_{as}\| < \lambda_{min}(K_d)\sqrt{\lambda_{min}((K_p)_s)}$. The minimal eigenvalue of the damping matrix, $\lambda_{min}(K_d)$, is roughly the same for the two grasps. The minimal eigenvalue of the symmetrized stiffness matrix, $\lambda_{min}((K_p)_s)$, corresponds to the grasp's rotational stiffness about its *center of compliance* (roughly located at the grasp's centroid). The rotational stiffness associated with a given preload level *increases* as the number of fingers increases from two to three. Thus $\lambda_{min}((K_p)_s)$ is larger in the three-finger grasp. The stability criterion therefore admits larger values of $\|(K_p)_{as}\|$, and hence larger values of ϕ in the three-finger grasp.

6 Oblique Loading Experiments

This section describes experiments validating the Hertz-Walton model in the simplest setting of a single compliant fingertip loaded against a rigid frictional plane.[7] The experiments determine how effectively the Hertz-Walton model can be used to predict the contact force developed under various oblique contact loading profiles. For each loading profile, the force-displacement measurements will be fitted to the Hertz-Walton model:

$$f_n = k_n(\delta_n)^{3/2} \quad \text{and} \quad f_t = \frac{k_t}{\sqrt{c}}(\delta_t)^{3/2} \qquad c = \delta_t/\delta_n, \tag{31}$$

where c is the slope of the linear loading profile, and k_n and k_t are constants that lump the material and geometric properties of the contacting bodies. This is the Hertz-Walton model

[7]The experiments were conducted in collaboration with A. Greenfield and H. Choset at CMU [35].

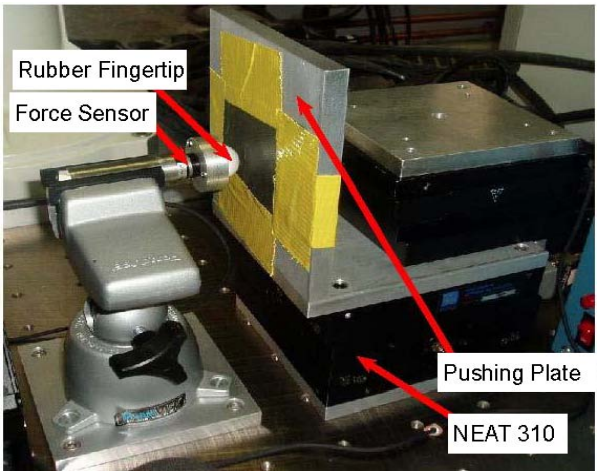

Figure 6: Experimental setup showing the compliant fingertip mounted to a static force sensor clamped to the experiment table. A two-axis positioning device drives the vertical pushing plate against the compliant fingertip.

specified in Section 2, except for the damping terms which are omitted since during the experiments the loading was applied very slowly with negligible damping. The experiments check the model validity for a variety of loading profiles, starting with normal loadings, continuing with oblique linear loadings, and then some piecewise linear loading paths.

Experimental setup: As shown in Figure 6, the three main components of the experimental system are a high precision positioning device, a force sensor, and a compliant fingertip. The positioning device is NEAT-310 made by New England Affiliated Technologies. It is a high precision positioning device consisting of two axis output stages. Each axis is individually driven by a 1 μm resolution stepper motor. The force sensor is the Nano17 force-torque sensor made by ATI Industrial Automation. This force sensor has a resolution of 1/1280 N on each force axis and is rated up to 50 N. The compliant fingertip material is a 1" diameter rubber ball available from McMaster-Carr as part number 96385K62. This material was chosen primary for its compliance which rates at 45-50 on the Shore A scale.[8] The main advantage of using such a compliant material is that the compliance of the rest of the system (i.e. force sensor and structural compliance) is negligible with respect to the rubber ball compliance.

In order to setup the experimental system, the rubber ball was cut into a half-ball, then

[8]Shore A is a scale for measuring Durometer hardness which is the international standard for measuring the hardness of rubber, plastic, and most nonmetallic materials. For instance, 40 on Shore A scale corresponds to the hardness of a common pencil eraser

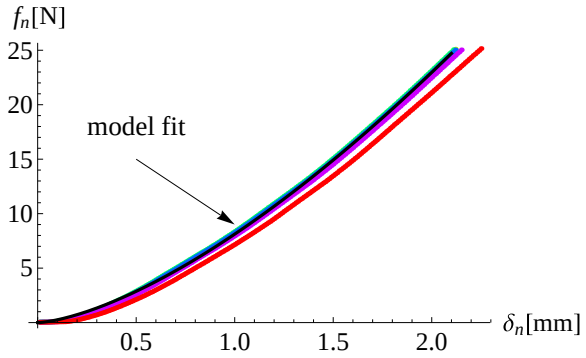

Figure 7: Force versus displacement measurements for ten normal loading profiles, overlayed with the Hertz model fit of $k_n = 8.119$ N/mm.

mounted onto a rigid plate attached to the force sensor (Figure 6). The force sensor was screwed to an aluminum tube, which was clamped by a rigid vice screwed to the experiment table (Figure 6). This setup held the compliant fingertip fixed with respect to the experiment table. The NEAT-310 positioning device was also screwed to the table. A horizontal aluminum plate was screwed to the top of the positioning device output stage, then a vertical aluminum plate was screwed to the horizontal plate (Figure 6). The vertical plate, covered with sandpaper to increase its contact friction, served as the planar "object" surface loaded against the compliant fingertip.

Normal loading path experiments: Ten normal loading experiments were conducted. Each experiment loaded the compliant fingertip up to 25 N in the contact normal direction. The Hertz contact model was then fitted to the force versus displacement measurements. The tangential component could not be estimated based on these experiments, since no tangential deflection was produced. The results of the ten experiments as well as the model fitted to these measurements are shown in Figure 7. In order to assess the quality of the fit, which visually appears highly accurate, statistics are shown in Table 1. The statistical quantities used in the table are described in Ref. [36]. The Hertz normal compliance model clearly fits the normal loading measurements very well.

Table 1: Normal loading statistics.

R^2	Mean Error	Mean Norm.	Max Error	Min Error
.9997	.1677 N	3.421%	.7523 N	-.8248 N

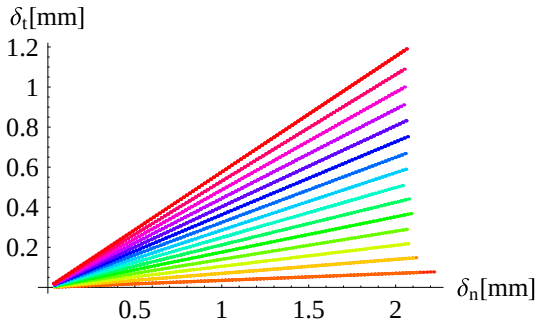

Figure 8: The linear loading profiles used in the experiments.

Oblique linear loading experiments: In these experiments the positioning device pushed the vertical plate against the compliant fingertip at a constant ratio between the normal and tangential deflections δ_n and δ_t. The compliant fingertip was loaded with fifteen oblique linear loading profiles, whose angles in the (δ_n, δ_t) plane ranged from 2° to 30° in increments of two degrees. Figure 8 depicts the fifteen linear loading profiles used in the experiments. Each of the fifteen loading profiles was repeated three times, giving a total of forty-five oblique loading experiments. Each experiment lasted until a normal force of 25 N developed at the compressed contact. The experimental measurements along with the model fitted to the data are shown in Figure 9. In the tangential direction, we normalized the tangential force f_t by the square root of the slope used in each particular loading path, $\sqrt{c} = \sqrt{\delta_t/\delta_n}$. This normalization allows visualization of the force versus displacement data solely as a function of δ_t, since $f_t\sqrt{c} = k_t\delta_t^{3/2}$ according to the Hertz-Walton model (31).

To assess the quality of the model fit, several statistics were generated for the fit in the normal and tangential directions. The statistics are shown in Table 2. Again the fit appears quite good, indicating that the Hertz-Walton model can adequately predict the compliant force developed under oblique linear loading profiles. Additionally, the parameter k_n agrees closely with the value fitted from the normal loading path experiments. This is not unexpected, since the normal loading profile is a special case of an oblique loading path.

Table 2: Oblique loading normal and tangential statistics.

	R^2	Mean Error	Mean Norm. Error	Max Error	Min Error
Normal	.9996	.2326 N	5.21%	1.187 N	-2.241 N
Tangential	.9977	.0482 N	13.02%	.1439 N	-.2036 N

Piecewise linear loading experiments: The last set of experiments tested the assumption

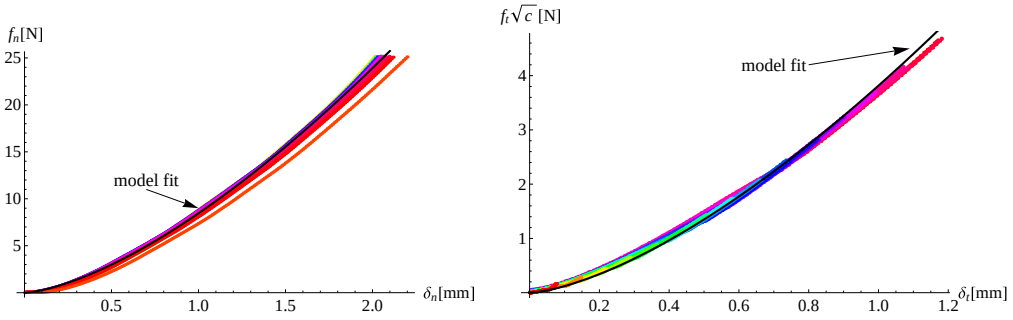

Figure 9: Component measurements data and model fit for oblique loading path experiments:
(a) Normal loading with $k_n = 8.458$ N/mm; (b) Tangential loading with $k_t = 3.814$ N/mm.

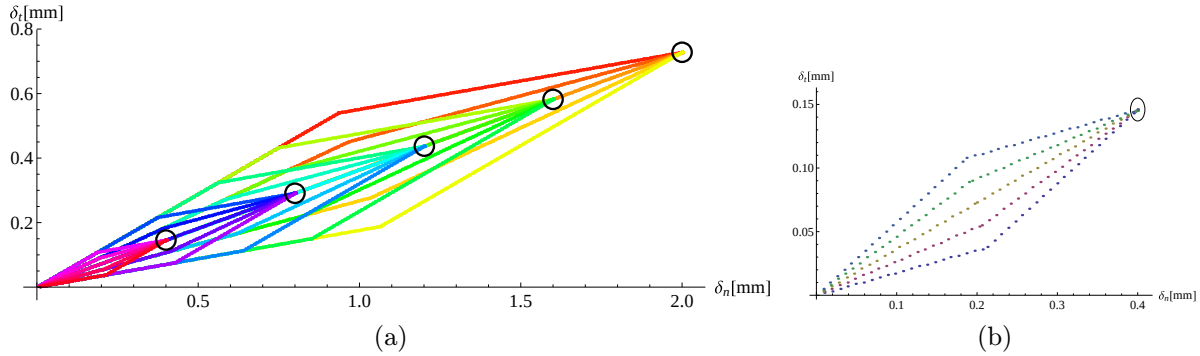

Figure 10: The piecewise linear loading paths of Set 1: (a) the five via points lie on a common linear loading path; (b) an enlargement of the five loading paths leading to the first via point.

made in Section 3, that closely matching loading profiles generate closely matching tangential traction fields. Three sets of piecewise linear loading paths, denoted Set 1, 2, and 3, were performed. Each piecewise linear path consisted of two linear segments. In each set of experiments, five via points were chosen in the (δ_n, δ_t) plane, equally spaced along a 20° linear loading path (Figure 10(a)). The five points are termed the *via points*. Five different loading paths converged on each via point at different angles. Each loading path was repeated twice, for a total of fifty experiments for each set. For instance, the twenty five loading paths used in Set 1, together with an enlargement of the five paths reaching the first via point, are depicted in Figure 10. In the piecewise linear loading paths of Set 1, the approach angle ranged from 10° to 30° in increments of five degrees. In Set 2 the approach angles ranged from 16° to 24° in smaller increments of two degrees. Finally, in Set 3 the approach angle

Table 3: The piecewise linear loading path dispersion statistics.

	Total Error	Mean Norm. Error
Set 1	10.28 N	1.8 %
Set 2	9.28 N	3.6 %
Set 3	4.61 N	1.0 %

ranged from 18° to 22° in yet smaller increments of one degree. The piecewise linear loading paths thus approach pure linear paths as one moves from Set 1 to Set 3.

The measured data points from all loading paths at the five via points are shown in Figure 11, along with fits to the linear loading path data in each experiment set. The data appears linear in the (f_n, f_t) plane due to the equivalent dependence of each force component on its respective displacement. Critically, *no model* which uses only (δ_n, δ_t) as its state information can fully predict the dispersion of the measured data at the five via points. Statistics characterizing the dispersion of these points are listed in Table 3. See Ref. [36] for a description of each statistic.

As seen in Figure 11, the dispersion of the data points decreases as the loading paths approach pure linear loading paths. For the large loading path variations in Set 1, the data is visibly spread apart. However, the mean normalized error characterizing this spread is only 1.8%. This small spread indicates that if the Hertz-Walton model is used to predict the forces for the piecewise linear loading paths at the five via points, on average the model would only be incorrect by 1.8%. The reason for the unexpected larger mean normalized error in Set 2 is that the zero displacement changed and the experiment begun in smaller displacements, and smaller forces. Therefore the means of the finger force magnitudes are also smaller than in the other sets, hence increasing the mean normalized error.

7 Conclusion

This paper considered the effect of natural material compliance on the stiffness and stability of frictional multi-contact arrangements. The paper introduced the Hertz-Walton contact model from the solid mechanics literature. Under an oblique linear loading of two quasi-rigid objects, the model provides a concise analytic formula for the force-displacement relationship at a frictional compliant contact. Based on the Hertz-Walton model, we obtained the stiffness matrices at the individual contacts. The main finding of the paper is that the individual contact stiffness matrices are *asymmetric* due to tangential stiffening with increased normal loading at the contacts. The composite grasp stiffness matrix of a multi-contact grasp was

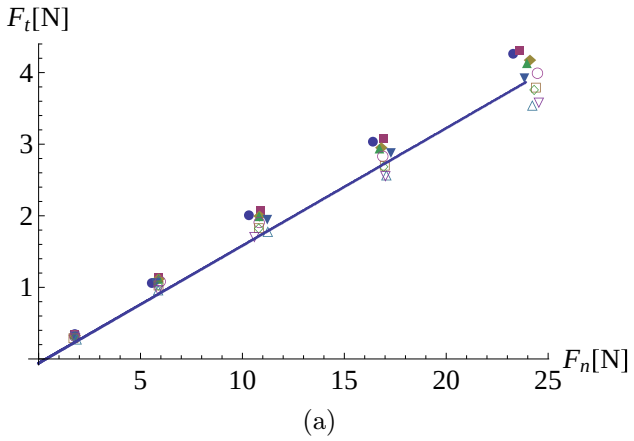

(a)

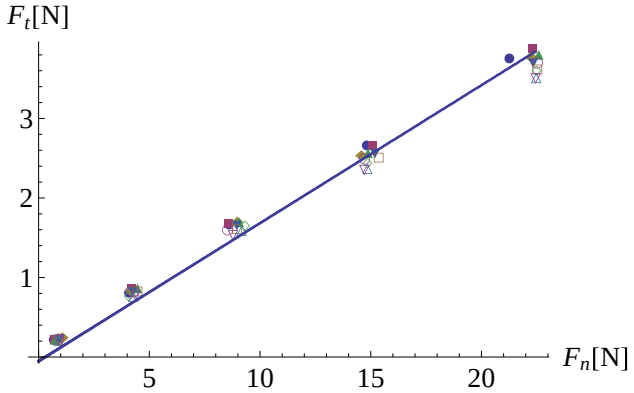

(b)

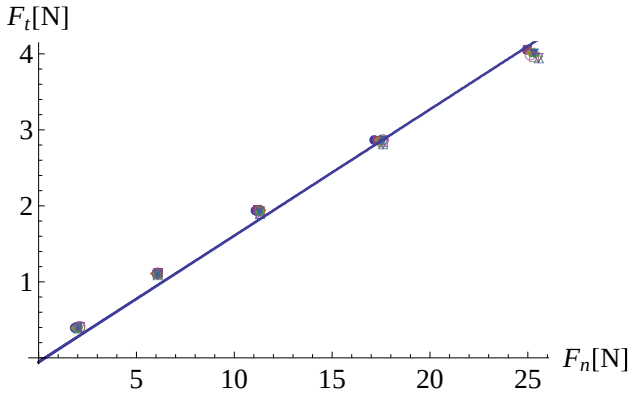

(c)

Figure 11: The piecewise linear loading paths via points data and model fit: (a) Set 1: 10°–30° range in 5° increments; (b) Set 2: 16°–24° range in 2° increments; (c) Set 3: 18°–22° range in 1° increments.

shown to be *asymmetric* as well, thus indicating that such grasps are *not* governed by any potential energy function. The paper then analyzed the grasp's linearized dynamics, and derived a consice condition for the local stability of an object held by frictional compliant contacts. Some qualitative guidelines for synthesizing compliantly stable grasps were derived and illustrated with examples. Finally, experiments validated the predictions of the Hertz-Walton contact model on a single compliant fingertip loaded with various oblique linear loading profiles.

The work reported in this paper is only the first stage of a larger research program. First and foremost, we are in the process of instrumenting an experimental system that will test the predictions of the Hertz-Walton contact model in full multi-contact settings. Second, the paper considered the compliant stability of an object $\mathcal{B}$ held by finger bodies, without any other external influences affecting the object $\mathcal{B}$. We are currently extending the grasp stability analysis to include gravity as well as small contact placement errors. Third, the bodies considered in this paper were assumed to lie on a frictionless supporting plane, such that the bodies interact via frictional forces parallel to the supporting plane. This assumption greatly simplified the analysis of the nonlinear grasp dynamics, since the object's motion were confined to the supporting plane. While many fixturing arrangements lie on a common supporting plane, most multi-finger grasping and locomotion applications are fully three-dimensional. In order to extend the work reported in this paper to three-dimensions, one must formulate Walton's tangential compliance model to linear loading profiles in three-dimensions, then work out the stability analysis along the lines considered here for two-dimensions. This major challenge will be explored in future work.

Finally, the Hertz-Walton contact model seems to provide excellent force-displacement predictions under oblique linear loading of the contacts. However, not all practical loading paths are of this nature. A major challenge would be to obtain an analytic lumped parameter contact model that will be valid under more general contact loading profiles. The work of Elata and Berryman [7] seems highly relevant in this context. These authors claim that by adding one state variable per contact, the *plastic strain* incurred during loading, an analytic force-displacement law can be obtained for completely general contact loading profiles.

Acknowledgements: We wish to thank Prof. David Elata for introducing us to the Hertz-Walton contact model. We also wish to thank Prof. Howie Choset and Aaron Greenfield for helping us conduct the experiments reported in the paper.

A Details of Grasp Stability Analysis

This appendix contains proofs of results stated in Section 4 and Section 5. The first results concerns the linearized grasp dynamics under the Hertz-Walton compliance model. We begin with a preliminary lemma concerning $D^2X_{r_i}$.

Lemma A.1. *Let $X_{r_i}(q) = R(\theta)r_i + d$ be the position of the i^{th} contact such that $q = (d, \theta)$ is $\mathcal{B}$'s configuration and $r_i \in \mathcal{B}$ is held fixed. The action of $D^2X_{r_i}^T(q)$ on f_i is the 3×3 matrix:*

$$D^2X_{r_i}^T(q)f_i = \begin{bmatrix} O & 0 \\ 0^T & -\boldsymbol{\rho}_i \cdot f_i \end{bmatrix},$$

where O is a 2×2 matrix of zeroes.

Proof: It can be verified that the Jacobian of $X_{r_i}(q)$ is the 2×3 matrix $DX_{r_i}(q) = [I\ J\boldsymbol{\rho}_i(\theta)]$, where I is a 2×2 identity matrix, $J = \left[\begin{smallmatrix} 0 & -1 \\ 1 & 0 \end{smallmatrix}\right]$, and $\boldsymbol{\rho}_i(\theta) = R(\theta)r_i$. To obtain a formula for $D^2X_{r_i}(q)$, we compute the derivative of $DX_{r_i}(q)$ along a c-space trajectory $q(t)$. Recall that $\mathcal{B}$'s velocity along $q(t)$ is denoted $\dot{q} = (v, \omega)$, where $v \in I\!R^2$ and $\omega \in I\!R$ are $\mathcal{B}$'s linear and angular velocities. Then $\frac{d}{dt}DX_{r_i}(q(t)) = \begin{bmatrix} O\ J\dot{R}r_i \end{bmatrix} = \begin{bmatrix} O\ -\boldsymbol{\rho}_i\omega \end{bmatrix}$, where we used the formula $\dot{R}r_i = \omega JRr_i$ and the identity $J^2 = -I$. The action of this derivative on f_i is: $\left(\frac{d}{dt}DX_{r_i}^T(q(t))\right)f_i = \begin{pmatrix} 0 \\ (-\boldsymbol{\rho}_i \cdot f_i)\omega \end{pmatrix}$. On the other hand, $\frac{d}{dt}DX_{r_i}(q(t)) = (D^2X_{r_i}(q))\dot{q}$ by the chain rule. Hence the action of $D^2X_{r_i}(q)$ on f_i is the 3×3 matrix:

$$D^2X_{r_i}^T(q)f_i = \begin{bmatrix} O & 0 \\ 0^T & -\boldsymbol{\rho}_i \cdot f_i \end{bmatrix},$$

where O is a 2×2 matrix of zeroes. □

The following proposition specifies the linearized grasp dynamics under the Hertz-Walton compliance model.

Proposition 4.1. *Let a quasi-rigid body $\mathcal{B}$ be held at an equilibrium grasp configuration, $q_0 = (d_0, \theta_0)$, by quasi-rigid finger bodies $\mathcal{A}_1, \ldots, \mathcal{A}_k$. Let $\Delta p_1 = q - q_0$ and $\Delta p_2 = \dot{q} - 0$. The* **linearized dynamics** *of $\mathcal{B}$ at $(q_0, 0)$ is given by*

$$\frac{d}{dt}\begin{pmatrix} \Delta p_1 \\ \Delta p_2 \end{pmatrix} = \begin{bmatrix} O_{3\times3} & I_{3\times3} \\ -M^{-1}(q_0)K_p(q_0, 0) & -M^{-1}(q_0)K_d(q_0, 0) \end{bmatrix}\begin{pmatrix} \Delta p_1 \\ \Delta p_2 \end{pmatrix}, \tag{32}$$

where K_p and K_d are the grasp stiffness and damping matrices. The grasp **stiffness matrix** *is the asymmetric 3×3 matrix:*

$$K_p(q_0, 0) = -\sum_{i=1}^{k}\left\{\tilde{K}_i(q_0) - \begin{bmatrix} O_{2\times2} & 0 \\ 0^T & \boldsymbol{\rho}_i(\theta_0) \cdot f_i \end{bmatrix} + G_i^T(q_0)\begin{bmatrix} f_i^n & f_i^t \\ -f_i^t & f_i^n \end{bmatrix} Dn_i(q_0)\right\}, \tag{33}$$

where $\tilde{K}_i(q_0)$ *is the* i^{th} *contact c-space stiffness matrix,* $\boldsymbol{\rho}_i(\theta_0)$ *is the* i^{th} *contact position relative to* $\mathcal{B}$*'s origin,* f_i *is the* i^{th} *contact force with components* (f_i^t, f_i^n)*, and* n_i *is the* i^{th} *contact normal* $(i = 1 \dots k)$*. The grasp* **damping matrix** *is the symmetric* 3×3 *matrix:*

$$K_d(q_0, 0) = \sum_{i=1}^{k} \delta_i^n(q_0) G_i^T(q_0) R_i(q_0) \begin{bmatrix} \frac{\partial \varphi_i^t}{\partial \dot{\delta}_i^t}(0) & 0 \\ 0 & \frac{\partial \varphi_i^n}{\partial \dot{\delta}_i^n}(0) \end{bmatrix} R_i^T(q_0) G_i(q_0), \tag{34}$$

where φ_i^t *and* φ_i^n *are the* i^{th} *tangential and normal damping functions evaluated at* $\dot{\delta}_i^t = \dot{\delta}_i^n = 0$ $(i = 1 \dots k)$*.*

Proof: First consider the linearization of $M^{-1}(p_1)$ and $C(p_1, p_2)$ in (12). The net wrench acting on $\mathcal{B}$, $\sum_{i=1}^k G_i^T f_i$, vanishes at $p_1 = q_0$. Moreover, $C(p_1, p_2)$ is quadratic and homogenous in p_2, therefore it vanishes at $p_2 = 0$. It follows from these two facts that the linearization of $M^{-1}(p_1)$ (which multiplies the term $\sum_{i=1}^k G_i^T f_i - C(p_1, p_2)$) and the linearization $C(p_1, p_2)$ both vanish at $(q_0, 0)$. Thus we only need to compute the matrices:

$$\begin{aligned} K_p(q_0, 0) &= -\frac{\partial}{\partial p_1}\Big|_{\substack{p_1 = q_0 \\ p_2 = 0}} \sum_{i=1}^k G_i^T(p_1) f_i(p_1, p_2) \\ K_d(q_0, 0) &= -\frac{\partial}{\partial p_2}\Big|_{\substack{p_1 = q_0 \\ p_2 = 0}} \sum_{i=1}^k G_i^T(p_1) f_i(p_1, p_2), \end{aligned}$$

where the minus signs will allow us to write the linearized dynamics in the standard form (17). First consider the matrix $K_p(q_0, 0)$. Since $G_i(p_1) = DX_{r_i}(p_1)$, the derivative $\frac{\partial}{\partial p_1} G_i^T(p_1) f_i(p_1, p_2)$ is given by

$$\frac{\partial}{\partial p_1} G_i^T(p_1) f_i(p_1, p_2) = D^2 X_{r_i}^T(p_1) f_i(p_1, p_2) + G_i^T \frac{\partial}{\partial p_1} f_i(p_1, p_2).$$

A formula for $D^2 X_{r_i}^T f_i$ is specified in Lemma A.1. Next consider the term $G_i^T \frac{\partial}{\partial p_1} f_i$. Using the notation $\boldsymbol{\delta}_i = (\delta_i^t, \delta_i^n)$ and $\dot{\boldsymbol{\delta}}_i = (\dot{\delta}_i^t, \dot{\delta}_i^n)$, the i^{th} contact force is given by

$$f_i(p_1, p_2) = R_i(p_1) \begin{pmatrix} f_i^t\big(\boldsymbol{\delta}_i(p_1), \dot{\boldsymbol{\delta}}_i(p_1, p_2)\big) \\ f_i^n\big(\boldsymbol{\delta}_i(p_1), \dot{\boldsymbol{\delta}}_i(p_1, p_2)\big) \end{pmatrix} \quad \text{where } R_i(p_1) = [t_i \, n_i].$$

Hence $\frac{\partial}{\partial p_1} f_i(p_1, p_2)$ is given by

$$\begin{aligned} &\tfrac{\partial}{\partial p_1} f_i(p_1, p_2) = \big(DR_i(p_1)\big) \begin{pmatrix} f_i^t(\boldsymbol{\delta}_i, \dot{\boldsymbol{\delta}}_i) \\ f_i^n(\boldsymbol{\delta}_i, \dot{\boldsymbol{\delta}}_i) \end{pmatrix} \\ &+ R_i(p_1) \left\{ \begin{pmatrix} \frac{\partial}{\partial \boldsymbol{\delta}_i} f_i^t(\boldsymbol{\delta}_i, \dot{\boldsymbol{\delta}}_i) \\ \frac{\partial}{\partial \boldsymbol{\delta}_i} f_i^n(\boldsymbol{\delta}_i, \dot{\boldsymbol{\delta}}_i) \end{pmatrix} D\boldsymbol{\delta}_i(p_1) + \begin{pmatrix} \frac{\partial}{\partial \dot{\boldsymbol{\delta}}_i} f_i^t(\boldsymbol{\delta}_i, \dot{\boldsymbol{\delta}}_i) \\ \frac{\partial}{\partial \dot{\boldsymbol{\delta}}_i} f_i^n(\boldsymbol{\delta}_i, \dot{\boldsymbol{\delta}}_i) \end{pmatrix} \tfrac{\partial}{\partial p_1} \dot{\boldsymbol{\delta}}_i(p_1, p_2) \right\}. \end{aligned} \tag{35}$$

Consider the first summand in (35). Since $t_i = J^T n_i$, the matrix $R_i = [t_i\, n_i]$ can be written as $R_i = [J^T n_i\, n_i]$, where $J = \left[\begin{smallmatrix} 0 & -1 \\ 1 & 0 \end{smallmatrix}\right]$. Thus $DR(q_0) = [J^T Dn_i(q_0)\, Dn_i(q_0)]$, and consequently $\big(DR_i(q_0)\big)\left(\begin{smallmatrix} f_i^t \\ f_i^n \end{smallmatrix}\right) = (f_i^t J^T + f_i^n I) Dn_i(q_0)$, where I is a 2×2 identity matrix. Next consider the second summand in (35). According to the Hertz-Walton model, the force components (f_i^t, f_i^n) are given by

$$\begin{pmatrix} f_i^t(\boldsymbol{\delta}_i, \dot{\boldsymbol{\delta}}_i) \\ f_i^n(\boldsymbol{\delta}_i, \dot{\boldsymbol{\delta}}_i) \end{pmatrix} = \begin{pmatrix} -h_i(\delta_i^t, \delta_i^n) \\ g_i(\delta_i^n) \end{pmatrix} + \delta_i^n \begin{pmatrix} -\varphi_i^t(\dot{\delta}_i^t) \\ \varphi_i^n(\dot{\delta}_i^n) \end{pmatrix}. \tag{36}$$

The derivative of (f_i^t, f_i^n) with respect to $\boldsymbol{\delta}_i = (\delta_i^t, \delta_i^n)$ at $(q_0, 0)$ is given by

$$\left.\begin{pmatrix} \frac{\partial}{\partial \boldsymbol{\delta}_i} f_i^t(\boldsymbol{\delta}_i, \dot{\boldsymbol{\delta}}_i) \\ \frac{\partial}{\partial \boldsymbol{\delta}_i} f_i^n(\boldsymbol{\delta}_i, \dot{\boldsymbol{\delta}}_i) \end{pmatrix}\right|_{\substack{p_1 = q_0 \\ p_2 = 0}} = K_i(q_0) + \left.\begin{bmatrix} 0 & -\varphi_i^t(\dot{\delta}_i^t) \\ 0 & \varphi_i^n(\dot{\delta}_i^n) \end{bmatrix}\right|_{\substack{p_1 = q_0 \\ p_2 = 0}} = K_i(q_0),$$

where we used the fact that $\dot{\delta}_i^t = \dot{\delta}_i^n = 0$ at $p_2 = 0$, and consequently $\varphi_i^t(0) = \varphi_i^n(0) = 0$. The Jacobian $D\boldsymbol{\delta}_i(p_1)$ in the second summand of (35) is given by $D\boldsymbol{\delta}_i = \left[\begin{smallmatrix} t_i^T \\ -n_i^T \end{smallmatrix}\right] G_i$ (see proof of Lemma 3.1). As for the third summand in (35), $\dot{\boldsymbol{\delta}}_i = \left[\begin{smallmatrix} t_i^T \\ -n_i^T \end{smallmatrix}\right] G_i p_2$. Hence $\frac{\partial}{\partial p_1}\dot{\boldsymbol{\delta}}_i(p_1, p_2) = 0$ at $p_2 = 0$. Substituting these terms in (35), then summing the expressions $D^2 X_{r_i}^T(p_1) f_i(p_1, p_2) + G_i^T \frac{\partial}{\partial p_1} f_i(p_1, p_2)$ over $i = 1 \ldots k$ gives

$$\begin{aligned} K_p(q_0, 0) &= -\tfrac{\partial}{\partial p_1}\Big|_{\substack{p_1 = q_0 \\ p_2 = 0}} \textstyle\sum_{i=1}^k G_i^T(p_1) f_i(p_1, p_2) \\ &= -\textstyle\sum_{i=1}^k \Big\{ G_i^T(q_0) R_i(q_0) K_i(q_0) \left[\begin{smallmatrix} t_i^T \\ -n_i^T \end{smallmatrix}\right] G_i(q_0) \\ &\quad - \begin{bmatrix} O & 0 \\ 0^T & \boldsymbol{\rho}_i(\theta_0) \cdot f_i \end{bmatrix} + G_i^T(q_0)(f_i^t J^T + f_i^n I) Dn_i(q_0) \Big\}, \end{aligned} \tag{37}$$

where we substituted $D^2 X_{r_i}^T(q_0) f_i = \left[\begin{smallmatrix} O & 0 \\ 0^T & -\boldsymbol{\rho}_i \cdot f_i \end{smallmatrix}\right]$ in accordance with Lemma A.1. Based on the proof of Lemma 3.1, $\tilde{K}_i = G_i^T(q_0) R_i(q_0) K_i(q_0) \left[\begin{smallmatrix} t_i^T \\ -n_i^T \end{smallmatrix}\right] G_i(q_0)$. Substituting for this term in (37) gives the formula:

$$K_p(q_0, 0) = -\sum_{i=1}^k \left\{ \tilde{K}_i(q_0) - \begin{bmatrix} O & 0 \\ 0^T & \boldsymbol{\rho}_i(\theta_0) \cdot f_i \end{bmatrix} + G_i^T(q_0)(f_i^t J^T + f_i^n I) Dn_i(q_0) \right\}.$$

Finally consider the matrix $K_d(q_0, 0)$. We have to compute the derivative:

$$\frac{\partial}{\partial p_2}\Big|_{\substack{p_1 = q_0 \\ p_2 = 0}} G_i^T(p_1) f_i(p_1, p_2) = G_i^T(p_1) \frac{\partial}{\partial p_2}\Big|_{\substack{p_1 = q_0 \\ p_2 = 0}} f_i(p_1, p_2).$$

Based on (36),

$$\frac{\partial}{\partial p_2} f_i(p_1,p_2) = R_i(p_1) \begin{bmatrix} -\delta_i^n(p_1)\cdot \frac{\partial}{\partial \dot{\delta}_i^t}\varphi_i^t(\dot{\delta}_i^t) & 0 \\ 0 & \delta_i^n(p_1)\cdot \frac{\partial}{\partial \dot{\delta}_i^n}\varphi_i^n(\dot{\delta}_i^n) \end{bmatrix} \frac{\partial}{\partial p_2}\dot{\boldsymbol{\delta}}_i(p_1,p_2).$$

Since $\dot{\boldsymbol{\delta}}_i = \begin{bmatrix} t_i^T \\ -n_i^T \end{bmatrix} G_i p_2$, we have that $\frac{\partial}{\partial p_2}\dot{\boldsymbol{\delta}}_i(p_1,p_2) = \begin{bmatrix} t_i^T \\ -n_i^T \end{bmatrix} G_i$. Hence

$$\begin{aligned} \frac{\partial}{\partial p_2}\Big|_{\substack{p_1=q_0 \\ p_2=0}} f_i(p_1,p_2) &= \delta_i^n(q_0) R_i(q_0) \begin{bmatrix} -\frac{\partial \varphi_i^t}{\partial \dot{\delta}_i^t}(0) & 0 \\ 0 & \frac{\partial \varphi_i^n}{\partial \dot{\delta}_i^n}(0) \end{bmatrix} \begin{bmatrix} t_i^T \\ -n_i^T \end{bmatrix} G_i(q_0) \\ &= -\delta_i^n(q_0) R_i(q_0) \begin{bmatrix} \frac{\partial \varphi_i^t}{\partial \dot{\delta}_i^t}(0) & 0 \\ 0 & \frac{\partial \varphi_i^n}{\partial \dot{\delta}_i^n}(0) \end{bmatrix} R_i^T(q_0) G_i(q_0), \end{aligned}$$

where we substituted $R_i^T = \begin{bmatrix} t_i^T \\ n_i^T \end{bmatrix}$. Summing over the k contacts,

$$\begin{aligned} K_d(q_0,0) &= -\frac{\partial}{\partial p_2}\Big|_{\substack{p_1=q_0 \\ p_2=0}} \sum_{i=1}^k G_i^T(p_1) f_i(p_1,p_2) \\ &= \sum_{i=1}^k \delta_i^n(q_0) G_i^T(q_0) R_i(q_0) \begin{bmatrix} \frac{\partial \varphi_i^t}{\partial \dot{\delta}_i^t}(0) & 0 \\ 0 & \frac{\partial \varphi_i^n}{\partial \dot{\delta}_i^n}(0) \end{bmatrix} R_i^T(q_0) G_i(q_0). \end{aligned}$$

□

The following lemma specifies the grasp stiffness matrix in the case where $\mathcal{B}$ is held along planar facets.

Lemma 5.1. *When $\mathcal{B}$ is held in equilibrium grasp along planar facets, the grasp stiffness matrix specified in eq. (33) becomes*

$$K_p(q_0,0) = -\sum_{i=1}^k \tilde{K}_i(q_0),$$

where $\tilde{K}_i(q_0)$ is the i^{th} c-space contact stiffness matrix ($i = 1 \ldots k$).

Proof: The stiffness matrix K_p is specified in (33) as

$$K_p(q_0,0) = -\sum_{i=1}^k \left\{ \tilde{K}_i(q_0) - \begin{bmatrix} O_{2\times 2} & 0 \\ 0^T & \boldsymbol{\rho}_i \cdot f_i \end{bmatrix} + G_i^T(q_0) \begin{bmatrix} f_i^n & f_i^t \\ -f_i^t & f_i^n \end{bmatrix} Dn_i(q_0) \right\}. \tag{38}$$

Consider the third summand in (38). The 2×3 Jacobian $Dn_i(q_0)$ is specified in eq. (16) as

$$Dn_i(q_0) = \frac{1}{r_{\mathcal{A}_i} + r_{\mathcal{B}_i} - \delta_i^n(q_0)} \left[I - n_i n_i^T,\ (r_{\mathcal{B}_i} + \boldsymbol{\rho}_i(\theta_0) \cdot n_i) J n_i \right],$$

where $J = \left[\begin{smallmatrix} 0 & -1 \\ 1 & 0 \end{smallmatrix} \right]$. Substituting $r_{\mathcal{B}_i} = \infty$ for the flat facets of $\mathcal{B}$ gives $Dn_i(q_0) = [O\ Jn_i]$. The third summand in K_p thus becomes

$$\begin{aligned}
&\textstyle\sum_{i=1}^k G_i^T(q_0) \left[\begin{smallmatrix} f_i^n & f_i^t \\ -f_i^t & f_i^n \end{smallmatrix} \right] Dn_i(q_0) \\
&= \textstyle\sum_{i=1}^k G_i^T(q_0) \left(f_i^t J^T + f_i^n I \right) [O\ Jn_i] = \left[O_{3\times 2},\ \sum_{i=1}^k G_i^T(q_0)(f_i^t n_i + f_i^n J n_i) \right] \\
&= \left[O_{3\times 2},\ \textstyle\sum_{i=1}^k G_i^T(q_0) J(f_i^t t_i + f_i^n n_i) \right] = \left[O_{3\times 2},\ \textstyle\sum_{i=1}^k G_i^T(q_0) J f_i \right],
\end{aligned}$$

where we used the relations $t_i = J^T n_i$ and $f_i = f_i^t t_i + f_i^n n_i$. The 2×3 Jacobian $G_i = DX_{r_i}(q_0)$ is given by $G_i = [I\ J\boldsymbol{\rho}_i]$. Substituting for G_i gives

$$\sum_{i=1}^k G_i^T(q_0) J f_i = \sum_{i=1}^k \left[\begin{smallmatrix} I \\ \boldsymbol{\rho}_i^T J^T \end{smallmatrix} \right] J f_i = \left[\begin{smallmatrix} J \sum_{i=1}^k f_i \\ \sum_{i=1}^k \boldsymbol{\rho}_i^T J^T J f_i \end{smallmatrix} \right] = \left[\begin{smallmatrix} \vec{0} \\ \sum_{i=1}^k \boldsymbol{\rho}_i \cdot f_i \end{smallmatrix} \right],$$

since $\sum_{i=1}^k f_i = \vec{0}$ at the equilibrium grasp. The curvature dependent term in K_p is thus

$$\sum_{i=1}^k G_i^T(q_0) \left[\begin{smallmatrix} f_i^n & f_i^t \\ -f_i^t & f_i^n \end{smallmatrix} \right] Dn_i(q_0) = \left[\begin{smallmatrix} O_{2\times 2} & 0 \\ 0^T & \sum_{i=1}^k \boldsymbol{\rho}_i \cdot f_i \end{smallmatrix} \right].$$

When this term is substituted into (38), one obtains that $K_p(q_0, 0) = -\sum_{i=1}^k \tilde{K}_i(q_0)$. □

The final proposition specifies the relation between the symmetric and asymmetric parts of the matrix A which guarantees the stability condition $\gamma < \sqrt{\alpha}\beta$.

Proposition 5.2. *Let $\mathcal{B}$ be held along planar facets in a k-finger grasp, such that $\delta_i^n(q_0) \cong \delta_c^n$ and $c_i \cong c$ for $i = 1 \ldots k$. Let $\alpha > 0$ and $\beta > 0$ for the given grasp. The stability condition $\gamma < \sqrt{\alpha}\beta$ is satisfied when A_s and A_{as} satisfy the condition:*

$$\|A_{as}\| < \kappa_d \frac{\lambda_{min}(\bar{M})}{\lambda_{max}(\bar{M})} \sqrt{\lambda_{min}(A_s)},$$

where A is specified in (27), κ_d is the damping parameter, and $\bar{M}$ is $\mathcal{B}$'s scaled inertia matrix.

Proof: Consider the condition $\gamma < \sqrt{\alpha}\beta$ specified in eq. (24). The term α can be written as

$$\alpha = \lambda_{min}(\bar{M}^{-\frac{1}{2}}(\bar{K}_p)_s\bar{M}^{-\frac{1}{2}}) = \min_{\|v\|=1}\left\{v^T\bar{M}^{-\frac{1}{2}}(\bar{K}_p)_s\bar{M}^{-\frac{1}{2}}v\right\}.$$

Substituting for $(\bar{K}_p)_s$ according to (25) gives

$$\lambda_{min}\big(\bar{M}^{-1/2}(\bar{K}_p)_s\bar{M}^{-1/2}\big) \geq \sqrt{\delta_c^n}\lambda_{min}\big(A_s\big)\cdot\min_{\|v\|=1}\left\{v^T\bar{M}^{-\frac{1}{2}}\big(\sum_{i=1}^{k}S^TG_i^TG_iS\big)\bar{M}^{-\frac{1}{2}}v\right\}, \quad (39)$$

where we substituted $R_iR_i^T = I$ for $i = 1\ldots k$. Without loss of generality, let the world and $\mathcal{B}$'s frames be located at the grasp's centroid. Under this assumption the position of each finger contact in $\mathcal{B}$'s frame is identical to its position in the world frame, $x_i = \boldsymbol{\rho}_i(\theta_0)$ for $i = 1\ldots k$, while $x_c = \vec{0}$. The Jacobian G_i is given by the 2×3 matrix $G_i = DX_{r_i} = [I\; Jx_i]$, where I is a 2×2 identity matrix and $J = \left[\begin{smallmatrix} 0 & -1 \\ 1 & 0 \end{smallmatrix}\right]$. Hence

$$\begin{aligned}
\textstyle\sum_{i=1}^k S^TG_i^TG_iS &= \textstyle\sum_{i=1}^k \begin{bmatrix} I & 0 \\ 0^T & 1/l_c \end{bmatrix}\begin{bmatrix} I \\ x_i^TJ^T \end{bmatrix}[I\; Jx_i]\begin{bmatrix} I & 0 \\ 0^T & 1/l_c \end{bmatrix} \\
&= \begin{bmatrix} kI & \frac{1}{l_c}J\sum_{i=1}^k x_i \\ \frac{1}{l_c}(\sum_{i=1}^k x_i)^TJ^T & \frac{1}{l_c^2}\sum_{i=1}^k\|x_i\|^2 \end{bmatrix} \\
&= k\begin{bmatrix} I & \frac{1}{kl_c}J\sum_{i=1}^k x_i \\ \frac{1}{kl_c}(\sum_{i=1}^k x_i)^TJ^T & \frac{1}{kl_c^2}\sum_{i=1}^k\|x_i\|^2 \end{bmatrix}.
\end{aligned}$$

Substituting $x_c = \frac{1}{k}\sum_{i=1}^k x_i = \vec{0}$ and $l_c^2 = \frac{1}{k}\sum_{i=1}^k\|x_i\|^2$ gives $\sum_{i=1}^k S^TG_i^TG_iS = kI_{3\times 3}$. The matrix $\sum_{i=1}^k S^TG_i^TG_iS$ is thus essentially the identity matrix. Substituting this matrix into (39) gives

$$\alpha = \lambda_{min}\big(\bar{M}^{-1/2}(\bar{K}_p)_s\bar{M}^{-1/2}\big) \geq k\sqrt{\delta_c^n}\lambda_{min}(A_s)\lambda_{min}(\bar{M}^{-1}),$$

where $\lambda_{min}(\bar{M}^{-1}) = \min_{\|v\|=1}\{v^T\bar{M}^{-1}v\}$. Next consider the quantity γ on the left side (24),

$$\begin{aligned}
\gamma^2 = \|\bar{M}^{-\frac{1}{2}}(\bar{K}_p)_{as}\bar{M}^{-\frac{1}{2}}\|^2 &= \lambda_{max}\left((\bar{M}^{-\frac{1}{2}}(\bar{K}_p)_{as}\bar{M}^{-\frac{1}{2}})^T\bar{M}^{-\frac{1}{2}}(\bar{K}_p)_{as}\bar{M}^{-\frac{1}{2}}\right) \\
&= \lambda_{max}\left(\bar{M}^{-\frac{1}{2}}(\bar{K}_p)_{as}^T\bar{M}^{-1}(\bar{K}_p)_{as}\bar{M}^{-\frac{1}{2}}\right).
\end{aligned}$$

In general, when P and Q are symmetric matrices, $\lambda_{max}(P^TQP) \leq \lambda_{max}(Q)\lambda_{max}(P^TP)$. Applying this inequality twice gives

$$\begin{aligned}
\|\bar{M}^{-\frac{1}{2}}(\bar{K}_p)_{as}\bar{M}^{-\frac{1}{2}}\|^2 &\leq \lambda_{max}(\bar{M}^{-1})\cdot\lambda_{max}\left(\bar{M}^{-\frac{1}{2}}(\bar{K}_p)_{as}^T(\bar{K}_p)_{as}\bar{M}^{-\frac{1}{2}}\right) \\
&\leq \lambda_{max}^2(\bar{M}^{-1})\cdot\lambda_{max}\left((\bar{K}_p)_{as}^T(\bar{K}_p)_{as}\right).
\end{aligned}$$

Substituting for $(\bar{K}_p)_{as}$ according to (26) gives

$$\|\bar{M}^{-\frac{1}{2}}(\bar{K}_p)_{as}\bar{M}^{-\frac{1}{2}}\|^2 \leq$$
$$\delta_c^n \lambda_{max}^2(\bar{M}^{-1})\|A_{as}\|^2 \cdot \max_{\|v\|=1}\Big\{v^T\big(\sum_{i=1}^k S^T G_i^T G_i S\big)^T\big(\sum_{i=1}^k S^T G_i^T G_i S\big)v\Big\}.$$

Since $\sum_{i=1}^k S^T G_i^T G_i S = kI$, we obtain that

$$\gamma = \|\bar{M}^{-1/2}(\bar{K}_p)_{as}\bar{M}^{-1/2}\| \leq k\sqrt{\delta_c^n}\lambda_{max}(\bar{M}^{-1})\|A_{as}\|.$$

When the upper bound on γ is combined with the lower bound on α, the condition $\gamma < \sqrt{\alpha}\beta$ is implied by the inequality:

$$\|A_{as}\| < \kappa_d \frac{\lambda_{min}(\bar{M})}{\lambda_{max}(\bar{M})}\sqrt{\lambda_{min}(A_s)},$$

where we canceled the common factor $k\sqrt{\delta_c^n}$ from both sides of the inequality and substituted $\lambda_{min}(\bar{M}^{-1}) = 1/\lambda_{max}(\bar{M})$ and $\lambda_{max}(\bar{M}^{-1}) = 1/\lambda_{min}(\bar{M})$. □

B Experiment Statistical Quantities

Normal and oblique loading path statistics:

1. R^2- coefficient of determination as reported by Mathematica ©.
2. Mean absolute error: $\frac{1}{n}\sum_{i=1}^n \|f_{d_i} - f_{m_i}(\delta_t, \delta_n)\|$, where f_{d_i} is the i^{th} force data point, of either normal force or tangential force, f_{m_i} is the model's prediction of force, and n is the number of data points.
3. Mean normalized absolute error: $\frac{1}{n}\sum_{i=1}^n \|\frac{f_{d_i} - f_{m_i}(\delta_t,\delta_n)}{f_{m_i}}\|$.
4. Maximal error: $\max_i(f_{d_i} - f_{m_i})$.
5. Minimal error: $\min_i(f_{d_i} - f_{m_i})$.

Piecewise linear loading path statistics:

1. Total error: $\sum_i \sum_j \|(f_{n_{ij}}, f_{t_{ij}}) - (\mu_{n_j}, \mu_{t_j})\|_2$, where $(f_{n_{ij}}, f_{t_{ij}})$ is the i^{th} force data point at the j^{th} convergence point with normal and tangential component respectively and (μ_{n_j}, μ_{t_j}) is the mean force at the j^{th} convergence point.
2. Mean normalized error: $\frac{1}{n}\sum_i \sum_j \frac{\|(f_{n_{ij}}, f_{t_{ij}}) - (\mu_{n_j}, \mu_{t_j})\|_2}{\|(\mu_{n_j}, \mu_{t_j})\|_2}$.

References

[1] A. Bicchi. Hands for dexterous manipulation and robust grasping: A difficult road toward simplicity. *IEEE Trans. on Robotics and Automation*, 16(6):652–662, 2000.

[2] P. Campbell. *Basic Fixture Design.* Industrial Press, New York, 1994.

[3] H. Choi and M. Koc. Design and feasibility tests of a flexible gripper based on inflatable rubber pockets. *Int. J. of Machine Tools and Manufacture*, 46:1350–1361, 2006.

[4] Y.-C. Chou, V. Chandru, and M. M. Barash. A mathematical approach to automatic configuration of machining fixtures: Analysis and synthesis. *ASME J. of Engineering for Industry*, 111:299–306, 1989.

[5] P. Y. Chua, T. Ilschner, and D. G. Caldwell. Robotic manipulation of food products—a review. *Industrial Robot: An International Journal*, 30:345–354, 2003.

[6] M. R. Cutkosky and I. Kao. Computing and controlling the compliance of a robotic hand. *IEEE Trans. on Robotics and Automation*, 5(2):151–165, 1989.

[7] D. Elata and J. G. Berryman. Contact force-displacement laws and the mechanical behavior of random packs of identical spheres. *Mechanics of Materials*, 24:229–240, 1996.

[8] B. Fang, R. E. DeVor, and S. G. Kapoor. An elastodynamic model of frictional contact and its influence on the dynamics of a worpiece-fixture system. *ASME J. of Manufacturing Science and Engineering*, 123:481–489, 2001.

[9] P. Flores, M. Machado, M. T. Silva, and J. M. Martins. On the continuous contact force models for soft materials in multibody dynamics. *Multibody System Dynamics*, 25:357–375, 2011.

[10] Y. Funahashi, T. Yamada, M. Tate, and Y. Suzuki. Grasp stability analysis considering the curvatures at contact points. In *IEEE Int. Conf. on Robotics and Automation*, pages 3040–3046, 1996.

[11] J. Halling. *Principals of Tribology.* Macmillan, London, 1975.

[12] K. Harada and M. Kaneko. A sufficient condition for manipulation of enveloping family. *IEEE Trans. on Robotics and Automation*, 18(4):597–607, 2002.

[13] P. Hartman. *Ordinary Differential Equations.* Birkaauser, Boston, MA., 1982.

[14] H. Hertz. On the contact of elastic solids. In *Miscellaneous Papers by H. Hertz (1882)*. Macmillan, London, 1896.

[15] M. W. Hirsch and S. Smale. *Differential Equations, Dynamical Systems, and Linear Algebra*. Academic Press, 1974.

[16] M. J. Hockenberger and E. C. De Meter. Effect of machining fixture design parameters on workpiece displacement. *Manufacturing Review*, 8(1):22–32, 1995.

[17] E. G. Hoffman. *Jig and Fixture Design*. Delmar Publishers, Albany, NY, 1991.

[18] W. S. Howard and V. Kumar. On the stability of grasped objects. *IEEE Trans. on Robotics and Automation*, 12(6):904–917, 1996.

[19] T. Inoue and S. Hirai. Elastic model of deformable fingertip for soft-fingered manipulation. *IEEE Trans. on Robotics*, 22(6):1273–1279, 2006.

[20] K. L. Johnson. *Contact Mechanics*. Cambridge University Press, 1985.

[21] H. M. Lankarani and P. E. Nikravesh. Continuous contact force models for impact analysis in multibody systems. *Nonlinear Dynamics*, (5):193–207, 1994.

[22] B. Li and S. N. Melkote. An elastic contact model for the prediction of workpiece-fixture contact forces in clamping. *ASME J. of Manufacturing Science and Engineering*, 121:485–493, 1999.

[23] Q. Lin, J. W. Burdick, and E. Rimon. Computation and analysis of natural compliance in grasping and fixturing arrangements. *IEEE Trans. on Robotics and Automation*, 20(4):651–667, 2004.

[24] Q. Lin, J. W. Burdick, and E. Rimon. Constructing minimum deflection fixture arrangements using frame invariant norms. *IEEE Trans. on Automation Science and Engineering*, 3(3):272–286, 2006.

[25] R. D. Mindlin. Compliance of elastic bodies in contact. *Trans. of the ASME*, 71:A–259, 1949.

[26] R. D. Mindlin and H. Deresiewicz. Elastic spheres in contact under varying oblique forces. *ASME J. of Applied Mechanics*, 20:327–344, 1953.

[27] D. J. Montana. The kinematics of contact with compliance. In *IEEE Int. Conf. on Robotics and Automation*, pages 770–774, 1988.

[28] D. J. Montana. Contact stability for two-fingered grasps. *IEEE Trans. on Robotics and Automation*, 8(4):421–230, 1992.

[29] V.-D. Nguyen. Constructing force-closure grasps. *The Int. J. of Robotics Research*, 7(3):3–16, 1988.

[30] T. Omata and K. Nagata. Rigid body analysis of the indeterminate grasp force in power grasps. *IEEE Trans. on Robotics and Automation*, 16(1):46–54, 2000.

[31] A. Pettersson, S. Davis, J. O. Gray, T. J. Dodd, and T. Ohlsson. Design of a magnetorheological robot gripper for handling of delicate food products with varying shapes. *J. of Food Engineering*, 98:332–338, 2010.

[32] E. Rimon, J. W. Burdick, and T. Omata. A polyhedral bound on the indeterminate contact forces in fixturing and grasping arrangements. *IEEE Trans. on Robotics and Automation*, 22(2):240–255, 2006.

[33] E. Rimon, S. Shoval, and A. Shapiro. Design of a spider robot for motion with quasistatic force constraints. *Autonomous Robots*, 10:279–296, 2001.

[34] A. Shapiro. Stability of second-order asymmetric linear systems with application to robot grasping. *ASME J. of Applied Mechanics*, 72(6):966–968, 2005.

[35] A. Shapiro, A. Greenfield, and H. Choset. Frictional compliance model development and experiments for snake robot climbing. In *IEEE Int. Conf. on Robotics and Automation*, pages 574–579, 2007.

[36] A. Shapiro, E. Rimon, and A. Ohev-Zion. On the mechanics of natural compliance in frictional contacts and its effect on grasp stiffness and stability. Tech. report, Dept. of ME, Ben Gurion University, robotics.bgu.ac.il, Oct. 2012.

[37] P. R. Sinha and J. M. Abel. A contact stress model for multifinger grasps of rough objects. *IEEE Trans. on Robotics and Automation*, 8(1):7–22, 1992.

[38] R. H. Smith. *Analyzing Friction in the Design of Rubber Products and Their Paired Surfaces*. CRC Press, 2008.

[39] J. Tian and Y.-B. Jia. Modeling deformable shell-like objects grasped by a robot hand. In *IEEE Int. Conf. on Robotics and Automation*, pages 1297–1302, 2009.

[40] C. D. Tsai and I. Kao. The latency model for viscoelastic contact interface in robotics: Theory and experiments. In *IEEE Int. Conf. on Robotics and Automation*, pages 1291–1296, 2009.

[41] C. D. Tsai, I. Kao, N. Sakamoto, M. Higashimori, and M. Kaneko. Applying viscoelastic contact modeling to grasping task: an experimental case study. In *IEEE/RSJ Int. Conf. on Intelligent Robots and Systems (IROS)*, pages 3737–3743, 2008.

[42] C. D. Tsai, I. Kao, A. Shibata, K. Yoshimoto, M. Higashimori, and M. Kaneko. Experimental study of creep response of viscoelastic contact interface under force control. In *IEEE/RSJ Int. Conf. on Intelligent Robots and Systems (IROS)*, pages 4275–4280, 2010.

[43] E. J. van Henten, J. Hemming, B. A. J. van Tuijl, J. G. Kornet, J. Meuleman, J. Bontsema, and E. A. van Os. An autonomous robot for harvesting cucumbers in greenhouses. *Autonomous Robots*, 13:241–258, 2002.

[44] K. Walton. The oblique compression of two elastic spheres. *J. of the Mechanics and Physics of Solids*, 26:139–150, 1978.

[45] K. Walton. The effective elastic moduli of a random packing of spheres. *J. of the Mechanics and Physics of Solids*, 35:213–226, 1987.

[46] Y.-T. Wang and V. Kumar. Simulation of mechanical systems with multiple frictional contacts. *ASME J. of Mechanical Design*, 116:571–579, 1994.

[47] C. H. Xiong, Y. F. Li, H. Ding, and Y.-L. Xiong. On the dynamic stability of grasping. *The Int. J. of Robotics Research*, 18(9):951–958, 1999.

[48] C.-H. Xiong, M. Y. Wang, Y. Tang, and Y.-L. Xiong. Compliant grasping with passive forces. *J. of Robotics Systems*, 22(5):271–285, 2005.

[49] N. Xydas, M. Bhagavat, and I. Kao. Study of soft-finger contact mechanics using finite elements analysis and experiments. In *IEEE Int. Conf. on Robotics and Automation*, pages 2179–2184, 2000.

[50] N. Xydas and I. Kao. Modeling of contact mechanics and friction-limit-surfaces for soft fingers in robotics, with experimental results. *The Int. J. of Robotics Research*, 18(8):941–950, 1999.